Diffusion Theory Model of the Neutron Number Probability Distribution in a Subcritical Multiplying Assembly

J. E. M. Saxby[1], Anil K. Prinja[1,2], M. D. Eaton[1]

[1] *Nuclear Engineering Group, Department of Mechanical Engineering, Imperial College London, Exhibition Road, London SW7 2AZ, UK*

[2] *Department of Nuclear Engineering, University of New Mexico, Albuquerque, NM 87131, USA*

© *British Crown Owned Copyright 2017/AWE*

Abstract

The probability distribution of neutron numbers in a symmetric subcritical reflected fissile sphere is numerically obtained using a one-speed diffusion approximation to the underlying backward Master equation. Employing an accurate space-time discretisation scheme, the coupled but closed system of equations for the number probabilities is sequentially solved as a function of position and time of an injected neutron. This solution is then used to construct the corresponding distributions for a random intrinsic source of arbitrary multiplicity. Numerical results clearly demonstrate the importance of including spatial dependence in the neutron number probability distributions, which show complex spatial behaviours that cannot be encapsulated in a point model system. This is especially evident in the case of the multi-region model where the presence of a reflector is seen to alter the approach to steady state of the number probabilities, while the material interface has a significant effect on the magnitude of the probabilities, both locally and globally.

1. Introduction

Measurement and modelling of neutron multiplicity distributions play a key role in the identification and characterisation of small samples of special nuclear material that is important in the nonproliferation and safeguards space (Böhnel, 1985; Enqvist et al., 2006; Mattingly, 2012). A knowledge of the neutron multiplicity distribution makes possible the estimation of integral properties such the strength of the inherent random source, and the mass and composition of an unknown sample (Mattingly, 2012; Enqvist et al., 2006). Moreover, because the neutronic signature of fissile materials deviates from the Poisson distribution, multiplicity distributions can help distinguish background neutrons arising from (α, n) reactions from those arising from fission chains.

Computational analysis of neutron counting in nuclear safeguards, with detailed physical geometry representation and accounting for energy dependence of neutron interac-

Email address: j.saxby12@imperial.ac.uk (J. E. M. Saxby[1])

tions and source spectra, has largely relied on either analog Monte Carlo simulation of the branching process (Pozzi et al., 2003), which is expensive and primarily useful for benchmarking purposes, or on the construction of low-order statistical moments using deterministic codes to obtain parameters such as the Feynmann-Y counting statistic from which integral properties of the sample can be inferred (Mattingly, 2012). An alternative approach is provided by the underlying Master equation for the probability distribution of neutron number under general conditions, but the complexity of this formulation makes numerical solution intractable for distributions of large neutron numbers. However, as the Master equation is equivalent to a coupled but closed set of equations for the neutron number distribution of successively higher order, direct numerical solution becomes feasible if the order of the neutron number necessary to adequately characterise the distribution is not high, typically in the tens. These are precisely the conditions that arise when dealing with small, highly subcritical samples and hence the approach is relevant to nonproliferation and safeguards work. Thus far, however, numerical work based on the Master equation has been restricted to computing neutron and photon distributions in lumped or point systems for a single source realisation (Enqvist et al., 2006). While useful for developing insight into the statistics of neutron multiplication and quantifying the effect of random sources, lumped models are unable to describe spatial effects originating from nonuniformity in the distribution of fissile material and the presence of neutron reflectors and absorbers. To describe such nonlocal phenomena it is necessary to treat spatial dependence explicitly in the Master equation. The objective of this work is to develop such a generalisation using the one-speed diffusion approximation and demonstrate the feasibility of obtaining numerical solutions for neutron numbers of varying orders in planar and spherical geometries. We conclude this discussion on numerical methods by mentioning other methods which have been developed to compute the neutron number probability distributions. Work by Prasad and Snyderman (2012) developed a recursive point model for subcritical systems regarding the time-asymptotic neutron number probability distribution of neutrons which escape a multiplying medium and are therefore available for detection. Additionally, Abate and Whitt (1992); Williams (2016); Chambers et al. (2016) have used numerical inversion of the generating function transform to obtain the neutron number probability distributions. However, this technique has only been applied to lumped models and requires the generating function to be known in closed form. It is not yet clear if this approach can be efficiently extended to handle non-lumped systems.

In this paper, we develop a time dependent, spatially extensive backward model for the neutron number probabilities in the one-speed diffusion approximation and investigate it in both the case of a single initiating neutron and additionally a constantly emitting source. The distributions obtained are benchmarked using semi analytical solutions for special cases in the slab model for the single initiating neutron case. The numerical scheme is then applied to a one dimensional symmetric reflected fissile sphere containing an intrinsic random source of general multiplicity. Extensive numerical results are presented and discussed for the neutron number distributions in various subregions of the system, for different neutron injection locations as well as with a distributed source, that demonstrate unequivocally the importance of explicitly describing spatial

heterogeneities in complex multiplying media with weak sources.

2. Backward Master Equation Formulation

We consider a convex multiplying body of volume $V \subset \mathbb{R}^3$ with bounding surface $\partial D \subset \mathbb{R}^2$ in which the neutron population evolves stochastically with time subject to random scattering, parasitic capture, and fission events with known probability laws. Restricting considerations to single energy neutrons, so that the neutron phase space is characterised by spatial position $\vec{r} \in V$ and direction of travel $\vec{\Omega} \in S^2$, we define $p_n(R, t_f; \vec{r}, \vec{\Omega}, t)$, $n = 0, 1, 2 \cdots$, as the probability of finding n neutrons in phase space region $R \subset V \times S^2$ at a time t_f conditioned on a single neutron existing in the body at an earlier time t at position $\vec{r}$ with direction vector $\vec{\Omega}$. Then, under the reasonable assumption that the neutron population evolves as a Markov process, $p_n(\cdots)$ satisfies the Chapmann-Kolmogorov equation or, when expressed in differential form, the more commonly known backward Master equation (Pál, 1962; Bell, 1965; Pázsit and Pál, 2008). The backward Master equation is an open system of coupled nonlinear integro-differential equations for the number distribution, and is more useful when expressed in terms of the probability generating function $G(R, t_f, z; \vec{r}, \vec{\Omega}, t)$ defined by the z-transform (Bell, 1965):

$$G(R, t_f, z; \vec{r}, \vec{\Omega}, t) = \sum_{n=0}^{\infty} z^n p_n(R, t_f; \vec{r}, \vec{\Omega}, t), \tag{1}$$

or, more conveniently, in terms of the modified generating function:

$$\tilde{G}(R, t_f, z; \vec{r}, \vec{\Omega}, t) = 1 - G(R, t_f, z; \vec{r}, \vec{\Omega}, t). \tag{2}$$

Suppressing the explicit dependence on R and t_f for notational convenience, the governing equation for the generating function is given by Bell (1965):

$$-\frac{1}{v}\frac{\partial \tilde{G}(z; \vec{r}, \vec{\Omega}, t)}{\partial t} - \vec{\Omega}.\nabla \tilde{G}(z; \vec{r}, \vec{\Omega}, t) + \Sigma_t(\vec{r}, t)\tilde{G}(z; \vec{r}, \vec{\Omega}, t) = \bar{\nu}(\vec{r}, t)\Sigma_f(\vec{r}, t)\left[\int \tilde{G}(z; \vec{r}, \vec{\Omega}', t)\frac{d\vec{\Omega}'}{4\pi}\right]$$
$$+ \Sigma_s(\vec{r}, t)\int \tilde{G}(z; \vec{r}, \vec{\Omega}', t)\frac{d\vec{\Omega}'}{4\pi} - \sum_{k=2}^{K}\frac{(-1)^k}{k!}\chi_k(\vec{r}, t)\Sigma_f(\vec{r}, t)\left[\int \tilde{G}(z; \vec{r}, \vec{\Omega}', t)\frac{d\vec{\Omega}'}{4\pi}\right]^k, \; t \leq t_f, \tag{3}$$

where Σ_t is the total cross section which is the sum of scattering, Σ_s, capture, Σ_c, and fission, Σ_f, cross sections. With $p_k, k = 0, 1, \cdots K$, defined as the probability that k neutrons emerge from a fission event, in other words, the neutron multiplicity, the factorial moments are given by $\chi_k = \sum_{i=0}^{K} i(i-1)(i-2)...(i-k+1)p_i$ and are defined such that $\chi_2/2!$ is the mean number of pairs, $\chi_3/3!$ is the mean number of triplets and so on. The nonlinear terms in Eq.(3), of highest degree equal to the maximum number of neutrons K emitted in fission, reflect the underlying branching process and is a source of significant complication for numerical solutions of the backward model, which will be discussed at length later in this paper. In addition to single energy neutrons and the assumption of isotropic scattering, it is assumed that fission neutrons

are uncorrelated in angle.

The auxiliary conditions on the neutron number distribution for a single initiating neutron comprise the final time condition:

$$p_n(R, t_f; \vec{r}, \vec{\Omega}, t_f) = \delta_{n,1}\, \mathcal{I}_R(\vec{r}, \vec{\Omega}) + \delta_{n,0}\, [1 - \mathcal{I}_R(\vec{r}, \vec{\Omega})], \tag{4}$$

where $\mathcal{I}_R(\vec{r}, \vec{\Omega})$ is the indicator function defined to be unity for $(\vec{r}, \vec{\Omega}) \in R$ and zero otherwise, and the boundary condition:

$$p_n(R, t_f; \vec{r}, \vec{\Omega}, t) = \delta_{n,0}, \quad \vec{r} \in \partial D,\ \vec{e} \cdot \vec{\Omega} > 0, \tag{5}$$

where $\vec{e}$ is the outward unit normal on the system boundary. Using the definition of the generating function, the corresponding final time and boundary conditions on $\tilde{G}$ are readily determined to be:

$$\tilde{G}(z; \vec{r}, \vec{\Omega}, t_f) = (1 - z)\, \mathcal{I}_R(\vec{r}, \vec{\Omega}), \tag{6}$$

and:

$$\tilde{G}(z; \vec{r}, \vec{\Omega}, t) = 0, \quad \vec{r} \in \partial D,\ \vec{e} \cdot \vec{\Omega} > 0,\ t < t_f. \tag{7}$$

We note from Eq.(1) that $G(R, t_f, z = 0; \vec{r}, \vec{\Omega}, t) = p_0(R, t_f; \vec{r}, \vec{\Omega}, t)$ represents the extinction probability, that is, the probability of finding no neutrons in R at a time t_f, given that a single neutron was introduced to the system at an earlier time t, with position $\vec{r}$ and direction vector $\vec{\Omega}$. It follows that $\tilde{G}(R, t_f, z = 0; \vec{r}, \vec{\Omega}, t) = 1 - p_0(R, t_f; \vec{r}, \vec{\Omega}, t)$ is the survival probability, that is, the probability of finding a non-zero number of neutrons in R at a time t_f given one initial neutron. Taken in the limit $t \to \infty$, the survival probability gives rise to the probability of initiation (POI) or divergence probability, a quantity which is non-zero for super-critical systems and of great relevance to the safety of nuclear systems. This will come to be useful later when we derive higher order number probability equations, as the survival probability will be an input to each of these equations and will lead to a significant simplification when calculating the derivatives and for numerical implementation.

For numerical expediency, we will assume in the rest of this paper that the physical properties of the medium (cross sections, multiplicities) are independent of time. Under these conditions, the solution is invariant to arbitrary translations of the time variable, meaning that it depends only on the time difference $s = t_f - t \geq 0$ and not on the initial and final times separately. Further assuming isotropic scattering and that the physical properties are spatially piecewise constant, Eq.(3) for the generating function can then be expressed in terms of the forward-time variable s as:

$$\frac{1}{v}\frac{\partial \tilde{G}(z; \vec{r}, \vec{\Omega}, s)}{\partial s} - \vec{\Omega}.\nabla \tilde{G}(z; \vec{r}, \vec{\Omega}, s) + \Sigma_t(\vec{r}) \tilde{G}(z; \vec{r}, \vec{\Omega}, s) = \bar{\nu}(\vec{r}) \Sigma_f(\vec{r}) \left[\int \tilde{G}(z; \vec{r}, \vec{\Omega}', s) \frac{d\vec{\Omega}'}{4\pi} \right]$$
$$\Sigma_s(\vec{r}) \int \tilde{G}(z; \vec{r}, \vec{\Omega}', s) \frac{d\vec{\Omega}'}{4\pi} - \sum_{k=2}^{K} \frac{(-1)^k}{k!} \chi_k(\vec{r}) \Sigma_f(\vec{r}) \left[\int \tilde{G}(z; \vec{r}, \vec{\Omega}', s) \frac{d\vec{\Omega}'}{4\pi} \right]^k, \ s \geq 0, \tag{8}$$

with initial and boundary conditions now given by:

$$\tilde{G}(z;\vec{r},\vec{\Omega},0) = (1-z)\,\mathcal{I}_R(\vec{r},\vec{\Omega}), \tag{9}$$

and:

$$\tilde{G}(z;\vec{r},\vec{\Omega},s) = 0, \quad \vec{r}\in\partial D,\ \vec{e}\cdot\vec{\Omega}>0,\ s>0. \tag{10}$$

2.1. Incorporating an Intrinsic Random Source

The backward Master equation discussed above describes the development in time and phase space of the progeny of a single initial neutron, that is, a single neutron chain. While the resulting neutron number distribution provides valuable insight into the branching process and the conditions under which the population may become extinct or diverge asymptotically in time, a complete characterisation of the random neutron population in the presence of randomly emitting neutron sources inherent to the system, such as spontaneous fission, requires consideration of multiple concurrent chains. We note that spontaneous fission neutron multiplicity plays a key role in distinguishing the presence of fissile material from background neutrons in detection systems (Enqvist et al., 2006). An explicit source cannot be included in the backward Master equation formulation but the neutron number distribution from a single chain is an essential ingredient in constructing the corresponding distribution in the presence of a random intrinsic source, as we demonstrate next.

Consider a random and isotropically emitting intrinsic neutron source of strength $Q(t)$ and spatial distribution $w(\vec{r})$, normalised such that $\int_V w(\vec{r})dV = 1$, first switched on at earlier time t. Also, let q_k, $k = 1, 2\cdots K_Q$ be the source multiplicity distribution with normalisation $\sum_{k=1}^{K_Q} q_k = 1$. Then, the source generating function can be shown (Bell, 1965; Prinja, 2012) to satisfy the differential equation:

$$\frac{\partial G^{(Q)}(z,t_f|t)}{\partial t} = Q(t)\left[1-\sum_{k=1}^{K_Q} q_k \int_V dV\, w(\vec{r})\, G_0^k(z,t_f;\vec{r},t)\right] G^{(Q)}(z,t_f|\vec{r},t), \quad t_0\le t\le t_f, \tag{11a}$$

$$G^{(Q)}(z,t_f|\vec{r},t_f) = 1, \tag{11b}$$

where in Eq.(11a) we have defined:

$$G_0(z,t_f;\vec{r},t) = \frac{1}{4\pi}\int G(z,t_f;\vec{r},\vec{\Omega},t)\,d\vec{\Omega}. \tag{12}$$

Setting $G = 1-\tilde{G}$ in Eqs.(11a) & (12), introducing the factorial moments for the given source multiplicity distribution:

$$\chi_j^{(Q)} = \sum_{k=j}^{K_Q} k(k-1)(k-2)\cdots(k-j+1)\,q_k \tag{13}$$

and noting the normalisation of $w(\vec{r})$ gives the result:

$$\frac{\partial G^{(Q)}(z,t_f|t)}{\partial t} = -Q(t)\left[\sum_{k=1}^{K_Q}\frac{(-1)^k}{k!}\chi_j^{(Q)}(\vec{r})\int_V dV\, w(\vec{r})\,\tilde{G}_0^k(z,t_f;\vec{r},t)\right] G^{(Q)}(z,t_f|t), \quad t_0 \le t \le t_f, \tag{14a}$$

$$G^{(Q)}(z,t_f|t_f) = 1. \tag{14b}$$

Equations (14a) & (14b) can be readily solved for the source generating function:

$$G^{(Q)}(z,t_f|t) = \exp\left\{\int_t^{t_f} dt'\, Q(t')\left[\sum_{k=1}^{K_Q}\frac{(-1)^k}{k!}\chi_k^{(Q)}(\vec{r})\int_V dV\, w(\vec{r})\,\tilde{G}_0^k(z,t_f|\vec{r},t')\right]\right\}. \tag{15}$$

Assuming that the source strength and medium properties are time-independent, the solution depends on the initial and final times through the time difference $s = t_f - t$ only and Eqs.(14a) & (15) can be written as:

$$\frac{\partial G^{(Q)}(z,s)}{\partial s} = Q\left[\sum_{k=1}^{K_Q}\frac{(-1)^k}{k!}\chi_k^{(Q)}(\vec{r})\int_V dV\, w(\vec{r})\,\tilde{G}_0^k(z,s|\vec{r})\right] G^{(Q)}(z,s), \tag{16a}$$

$$G^{(Q)}(z,0) = 1, \tag{16b}$$

and

$$G^{(Q)}(z,s) = \exp\left\{Q\left[\sum_{k=1}^{K_Q}\frac{(-1)^k}{k!}\chi_k^{(Q)}(\vec{r})\int_0^{s} ds'\int_V dV\, w(\vec{r})\,\tilde{G}_0^k(z,s'|\vec{r})\right]\right\}. \tag{17}$$

where $0 \le s \le t_f - t_0$ is the time lapsed since the source was switched on.

Finally, for a singlet emitting source, $p_k = \delta_{k,1}$ so that $\chi_1^{(Q)} = 1, \chi_j^{(Q)} = 0, j \ge 2$, and the source generating function reduces to the well known Bartlett formula (Bell, 1965; Pázsit and Pál, 2008).

2.2. Master Equation in the Diffusion Approximation

To simplify the numerical solution of the equations for the number probabilities, which will be developed in subsequent sections, we assume that the neutron number distribution has weak angular dependence. Whilst we appreciate that the diffusion approximation is not accurate for the small systems considered herein, our main objective is to demonstrate that it is possible to include spatial dependence in the solutions for the neutron number probability equations. Of course, the goal is to model these systems in an energy dependent form using a transport model and we intend to address this in a forthcoming paper. Finally, we observe from Eq.(14a) that only the angle

integrated generating function corresponding to a single initiating neutron is required for the case of a random isotropically emitting intrinsic source.
Thus, we specifically assume that the generating function can be expressed as:

$$\tilde{G}(R, t_f, z; \vec{r}, \vec{\Omega}, t) \approx \tilde{G}_0(R, t_f, z; \vec{r}, t) + 3\vec{\Omega} \cdot \vec{\tilde{G}}_1(R, t_f, z; \vec{r}, t), \tag{18}$$

where $\tilde{G}_0$ is defined as in Eq.(12) and $\vec{G}_1$ as:

$$\vec{\tilde{G}}_1(R, t_f, z; \vec{r}, t) = \frac{1}{4\pi} \int \vec{\Omega}\, \tilde{G}(R, t_f, z; \vec{r}, \vec{\Omega}, t) d\vec{\Omega}. \tag{19}$$

Inserting this expansion in Eq.(3), taking zeroth and first angular moments, and manipulating the resulting equations gives for $\vec{G}_1$,

$$\vec{\tilde{G}}_1(R, t_f, z; \vec{r}, t) = \frac{1}{3\Sigma_t} \nabla \tilde{G}_0(R, t_f, z; \vec{r}, t) \tag{20}$$

which is just the adjoint Fick's law, and yields the following equation for the isotropic component of the generating function in forward-time notation:

$$\frac{1}{v} \frac{\partial \tilde{G}_0(z; \vec{r}, s)}{\partial s} - \nabla \cdot D \nabla \tilde{G}_0(z; \vec{r}, s) = \left(\bar{\nu} \Sigma_f(\vec{r}) - \Sigma_a(\vec{r}) \right) \tilde{G}_0(z; \vec{r}, s) - \Sigma_f \sum_{k=2}^{K} (-1)^k \frac{\chi_k}{k!} \tilde{G}_0^k(z; \vec{r}, s). \tag{21}$$

Here we have introduced the diffusion coefficient $D = 1/3\Sigma_t$ (Lewis and Miller, 1993). The initial condition is given by:

$$\tilde{G}_0(z; \vec{r}, 0) = (1 - z)\, \mathcal{I}_R(\vec{r}), \tag{22}$$

while Eqs.(10), (18) & (19) give the standard homogeneous Marshak condition at the boundary:

$$\frac{1}{4} \tilde{G}_0(z; \vec{r}, s) + \frac{D}{2} \vec{e} \cdot \nabla \tilde{G}_0(z; \vec{r}, s) = 0, \quad \vec{r} \in \partial D,\ s > 0. \tag{23}$$

In implementation, this condition is modified slightly in the usual way (Lewis and Miller, 1993) to ensure that the solution vanishes at the exact or transport corrected extrapolation distance given by $0.7104/\Sigma_t$ and not $2/(3\Sigma_t)$ which is implicit in Eq.(23). Equation (21) has the form of a nonlinear reaction-diffusion equation with a parameter z, the generating function transform variable, but although compact and stand-alone, it is not suitable for computational work. In the ensuing sections we will convert Eq.(21) to a coupled system of reaction-diffusion and pure-diffusion equations for the neutron number probabilities directly which are then solved numerically for the number distribution in various subregions of the physical domain, for both a single initiating neutron and a random intrinsic neutron source.

In closing this section we remark that by using a diffusion equation to describe the angle integrated generating function we are not arguing that the underlying discrete state

Markov process used to formulate the backward Master equation can be approximated by a continuous state Markov process (Pázsit and Pál, 2008). The linear in angle ansatz has been employed here merely as a mathematical device to construct a numerical solution of an otherwise complex problem, precisely as is traditionally done when constructing approximate solutions to the transport equation (Lewis and Miller, 1993). For this reason, one is not precluded from using higher order angular representations of the generating function, such as the P_N method, to obtain more accurate solutions. To be sure, the coefficients of such an expansion, of which Eq.(21) is the lowest meaningful order, cannot individually be interpreted as generating functions of reduced underlying number probabilities, but the cumulative expansion does constitute a valid representation of the generating function of the true neutron number probabilities. However, since the isotropic component is the only term in the angular expansion that survives in an infinite medium setting, $\tilde{G}_0$ may be considered as the generating function for the neutron number probabilities corresponding to an *isotropically* injected initiating neutron. Finally, we note that equations of the diffusion type for continuous Markov processes, more appropriately referred to as Fokker-Planck equations, do exist and may be viewed as the equivalent of Master equations for discrete processes (Van Kampen, 1981). In certain circumstances the latter may be mathematically approximated by the former because it is easier to solve the resulting equations and not because the two processes can be claimed to be equivalent (Van Kampen, 1981; Gillespie, 1992).

3. Equations for Individual Number Probabilities

To recover the neutron number probabilities discussed in the previous section would require first solving the generating function equation and then inverting the z-transform. Except in elementary cases where closed form solutions can be obtained (lumped model with approximated multiplicity distributions) this direct approach is not feasible in the non-lumped setting considered herein. It is conceivable that the generating function equation could be solved numerically, by discretising the transform variable in addition to the phase space variables, but accurately reconstructing the number probabilities from the discretised data does not appear to be practical. However, in the application of interest here, namely, highly subcritical fissile systems, the probability of obtaining neutron numbers in excess of a few tens is known to be vanishingly small. In this case, the approach demonstrated by Böhnel (1985) and Enqvist et al. (2006) for the lumped model is extensible to the non-lumped case, as we demonstrate next.

From the definition of the modified generating function $\tilde{G}$ given in Eqs.(1) and (2), it is readily shown that the number probabilities are related to the derivatives of $\tilde{G}$ through the relationship:

$$\begin{aligned} p_s(\vec{r},s) &= \tilde{G}_0(0;\vec{r},s), \\ p_n(\vec{r},s) &= -\frac{1}{n!}\left.\frac{\partial^n \tilde{G}_0(z;\vec{r},s)}{\partial z^n}\right|_{z=0}, \quad n \geq 1. \end{aligned} \tag{24}$$

Noting that the transform variable z does not appear explicitly in Eq.(21) for the generating function, equations for the individual neutron number probabilities can therefore be obtained in principle by taking the appropriate order derivative of Eq.(21), setting $z = 0$ and using Eq.(24). Proceeding in this way yields for p_n, $n \geq 1$:

$$\begin{aligned}\frac{1}{v}\frac{\partial p_n(\vec{r},s)}{\partial s} - D\nabla^2 p_n(\vec{r},s) = \big(\bar{\nu}\Sigma_f(\vec{r}) - \Sigma_a(\vec{r})\big)p_n(\vec{r},s) \\ - \Sigma_f(\vec{r})\sum_{k=2}^{K}(-1)^k\frac{\chi_k(\vec{r})}{k!}\left(-\frac{1}{n!}\right)\frac{\partial^n}{\partial z^n}\tilde{G}_0^k(z;\vec{r},s)\Big|_{z=0}.\end{aligned} \tag{25}$$

Further progress requires expressing the n^{th} derivative of the k^{th} power of $\tilde{G}$ in terms of the derivatives of $\tilde{G}$ which may then be expressed in terms of the number probabilities, thereby obtaining a closed and numerically solvable system. Before considering a general method for obtaining the derivatives of the nonlinear term, it is instructive to examine the structure of the equations for a few low order number probabilities for which the derivatives of the nonlinear terms are straightforward to construct.

Thus, setting $z = 0$ in Eq.(21) immediately yields the equation for the survival probability:

$$\begin{aligned}\frac{1}{v}\frac{\partial p_s(\vec{r},s)}{\partial s} - D\nabla^2 p_s(\vec{r},s) = \big(\bar{\nu}\Sigma_f(\vec{r}) - \Sigma_a(\vec{r})\big)p_s(\vec{r},s) \\ -\Sigma_f(\vec{r})\sum_{k=2}^{K}(-1)^k\frac{\chi_k(\vec{r})}{k!}p_s^k(\vec{r},s).\end{aligned} \tag{26}$$

Setting $n = 1$ in Eq.(25) gives for $p_1(\vec{r},s)$, the probability of finding 1 neutron in the system:

$$\begin{aligned}\frac{1}{v}\frac{\partial p_1(\vec{r},s)}{\partial s} - D\nabla^2 p_1(\vec{r},s) = \big(\bar{\nu}\Sigma_f(\vec{r}) - \Sigma_a(\vec{r})\big)p_1(\vec{r},s) \\ - \Sigma_f(\vec{r})\sum_{k=2}^{K}(-1)^k\frac{\chi_k(\vec{r})}{(k-1)!}p_s(\vec{r},s)^{(k-1)}p_1(\vec{r},s).\end{aligned} \tag{27}$$

Following the same methodology and evaluating the second derivative, we obtain for the two-neutron probability

$$\begin{aligned}\frac{1}{v}\frac{\partial p_2(\vec{r},s)}{\partial s} - D\nabla^2 p_2(\vec{r},s) = \big(\bar{\nu}\Sigma_f(\vec{r}) - \Sigma_a(\vec{r})\big)p_2(\vec{r},s) \\ + \frac{1}{2!}\Sigma_f(\vec{r})\sum_{k=2}^{K}(-1)^k\frac{\chi_k(\vec{r})}{(k-2)!}p_s(\vec{r},s)^{(k-2)}p_1(\vec{r},s)^2 \\ - \Sigma_f(\vec{r})\sum_{k=2}^{K}(-1)^k\frac{\chi_k(\vec{r})}{(k-1)!}p_s(\vec{r},s)^{(k-1)}p_2(\vec{r},s),\end{aligned} \tag{28}$$

and the three-neutron probability

$$\begin{aligned}\frac{1}{v}\frac{\partial p_3(\vec{r},s)}{\partial s} - D\nabla^2 p_3(\vec{r},s) &= \big(\bar{\nu}\Sigma_f(\vec{r}) - \Sigma_a(\vec{r})\big)p_3(\vec{r},s) \\ &- \Sigma_f \sum_{k=2}^{K}(-1)^k \frac{\chi_k(\vec{r})}{(k-1)!} p_s(\vec{r},s)^{(k-1)} p_3(\vec{r},s) \\ &+ \Sigma_f \sum_{k=2}^{K}(-1)^k \frac{\chi_k(\vec{r})}{(k-2)!} p_s(\vec{r},s)^{(k-2)} p_1(\vec{r},s) p_2(\vec{r},s) \\ &- \frac{1}{3!}\Sigma_f(\vec{r}) \sum_{k=2}^{K}(-1)^k \frac{\chi_k(\vec{r})}{(k-3)!} p_s(\vec{r},s)^{(k-3)} p_1(\vec{r},s)^3,\end{aligned} \tag{29}$$

The initial and boundary conditions for the number probabilities can be obtained from Eqs.(22), (23), and (24) as:

$$\begin{aligned} p_s(R;\vec{r},0) &= \mathcal{I}_R(\vec{r}) \\ p_n(R;\vec{r},0) &= \delta_{n,1}\,\mathcal{I}_R(\vec{r}), \quad n = 1,2,\cdots \end{aligned} \tag{30}$$

and the boundary condition

$$\begin{aligned} p_s(z;\vec{r},s) &= 0, \quad \vec{r}\in\partial D,\ s>0, \\ p_n(z;\vec{r},s) &= 0, \quad \vec{r}\in\partial D,\ s>0, \quad n = 1,2,\cdots \end{aligned} \tag{31}$$

A few observations are in order. It is evident that the equations for the number probabilities form a coupled sequence, starting with the equation for the survival probability which is homogeneous and nonlinear but independent of any higher order number probability. The equations for p_n, $n \geq 1$, on the otherhand, are linear but inhomogeneous, with number probabilities of order less than n appearing as source terms in the order n equation. Thus, in the numerical solution of the linear equations only the source terms need to be updated to obtain successively higher order number probabilities. It is also clear that each successive differentiation produces an equation which is increasingly complicated and the process quickly becomes unmanageable when calculating the neutron number probabilities by hand. Symbolic algebra codes have previously been used to generate higher order derivatives in the time-independent lumped case (Böhnel, 1985; Enqvist et al., 2006), however, this approach is not practical when considered in the context of numerical solution of the space and time dependent number probabilities. We have consequently developed a general algorithm for generating derivatives of the nonlinear term to arbitrary order that is described in detail in the appendix of this paper. As a result, the derivatives for up to the 50^{th} order for a general multiplicity model have been calculated. In situations in which the medium being considered is subcritical, so that relatively few number probabilities are required to account for the vast majority of neutrons in the system, our approach is efficient for generating numerical results, as will be demonstrated later in this paper. A reduction in the quantity of neutron number probabilities required to accurately represent the

system means it is possible to deal with a smaller number of coupled differential equations and thus makes the method detailed above far less computationally expensive.

The equations for the number probabilities in the presence of an intrinsic random source can be derived using a similar process to that described above in the single initiating neutron case. From the definition of the source generating function, $G^{(Q)}$, it is easily shown that the individual source number probabilities are related to the source generating function via the relation

$$\theta_n(s) = \frac{1}{n!} \left. \frac{\partial^n G^{(Q)}(z,s)}{\partial z^n} \right|_{z=0}, \quad n \geq 0 \tag{32}$$

Again, the transform variable z does not appear explicitly in Eq.(14a) for the source generating function, thus the individual source neutron number probabilities can be obtained by taking derivatives of Eq.(14a), setting $z = 0$ and using Eq.(32).

Once again, it is instructive to consider the source number probability equations for a few low orders to highlight the structure of the equations in order to facilitate the construction of a general method. Employing this for $n = 0$, gives the equation for the source extinction probability, θ_0 as

$$\frac{\partial \theta_0(s)}{\partial s} = Q(s) \left[\sum_{k=1}^{K_Q} \frac{(-1)^k}{k!} \chi_k^{(Q)}(\vec{r}) \int_V dV\, w(\vec{r})\, p_s^k(\vec{r},s) \right] \theta_0(s) \tag{33}$$

Performing the first derivative on Eq.(14a) gives for θ_1.

$$\begin{aligned} \frac{\partial \theta_1(s)}{\partial s} = & - Q(s) \left[\sum_{k=1}^{K_Q} \frac{(-1)^k}{(k-1)!} \chi_k^{(Q)}(\vec{r}) \int_V dV\, w(r) p_s^{(k-1)}(\vec{r},s) p_1(\vec{r},s) \right] \theta_0(s) \\ & + Q(s) \left[\sum_{k=1}^{K_Q} \frac{(-1)^k}{k!} \chi_k^{(Q)}(\vec{r}) \int_V dV\, w(r) p_s^k(\vec{r},s) \right] \theta_1(s) \end{aligned} \tag{34}$$

The second derivative, gives for θ_2

$$
\begin{aligned}
\frac{\partial\theta_2(s)}{\partial s} = & \frac{Q(s)}{2!}\left[\sum_{k=1}^{K_Q}\frac{(-1)^k}{(k-2)!}\chi_k^{(Q)}(\vec{r})\int_V dV w(r)p_s^{(k-2)}(\vec{r},s)p_1^2(\vec{r},s)\right]\theta_0(s) \\
& - Q(s)\left[\sum_{k=1}^{K_Q}\frac{(-1)^k}{(k-1)!}\chi_k^{(Q)}(\vec{r})\int_V dV w(r)p_s^{(k-1)}(\vec{r},s)p_2(\vec{r},s)\right]\theta_0(s) \\
& - Q(s)\left[\sum_{k=1}^{K_Q}\frac{(-1)^k}{(k-1)!}\chi_k^{(Q)}(\vec{r})\int_V dV w(r)p_s^{(k-1)}(\vec{r},s)p_1(\vec{r},s)\right]\theta_1(s) \\
& + Q(s)\left[\sum_{k=1}^{K_Q}\frac{(-1)^k}{k!}\chi_k^{(Q)}(\vec{r})\int_V dV w(r)p_s^{k}(\vec{r},s)\right]\theta_2(s)
\end{aligned}
\tag{35}
$$

and the third, θ_3

$$
\begin{aligned}
\frac{\partial\theta_3(s)}{\partial s} = & -\frac{Q(s)}{3!}\left[\sum_{k=1}^{K_Q}\frac{(-1)^k}{(k-3)!}\chi_k^{(Q)}(\vec{r})\int_V dV w(r)p_s^{(k-3)}(\vec{r},s)p_1^3(\vec{r},s)\right]\theta_0(s) \\
& + Q(s)\left[\sum_{k=1}^{K_Q}\frac{(-1)^k}{(k-2)!}\chi_k^{(Q)}(\vec{r})\int_V dV w(r)p_s^{(k-2)}(\vec{r},s)p_1(\vec{r},s)p_2(\vec{r},s)\right]\theta_0(s) \\
& - Q(s)\left[\sum_{k=1}^{K_Q}\frac{(-1)^k}{(k-1)!}\chi_k^{(Q)}(\vec{r})\int_V dV w(r)p_s^{(k-1)}(\vec{r},s)p_3(\vec{r},s)\right]\theta_0(s) \\
& + \frac{Q(s)}{2!}\left[\sum_{k=1}^{K_Q}\frac{(-1)^k}{(k-2)!}\chi_k^{(Q)}(\vec{r})\int_V dV w(r)p_s^{(k-2)}(\vec{r},s)p_1^2(\vec{r},s)\right]\theta_1(s) \\
& - Q(s)\left[\sum_{k=1}^{K_Q}\frac{(-1)^k}{(k-1)!}\chi_k^{(Q)}(\vec{r})\int_V dV w(r)p_s^{(k-1)}(\vec{r},s)p_2(\vec{r},s)\right]\theta_1(s) \\
& - Q(s)\left[\sum_{k=1}^{K_Q}\frac{(-1)^k}{(k-1)!}\chi_k^{(Q)}(\vec{r})\int_V dV w(r)p_s^{(k-1)}(\vec{r},s)p_1(\vec{r},s)\right]\theta_2(s) \\
& + Q(s)\left[\sum_{k=1}^{K_Q}\frac{(-1)^k}{k!}\chi_k^{(Q)}(\vec{r})\int_V dV w(r)p_s^{k}(\vec{r},s)\right]\theta_3(s)
\end{aligned}
\tag{36}
$$

With the initial condition obtained from Eq.(16b) as

$$
\theta_n(0) = \delta_{n,0}. \tag{37}
$$

There are, once more, points to note regarding these equations. Firstly, the equations are all linear and inhomogeneous: depending on the source probabilities for orders

less than n and also the single initiating neutron probabilities, p_m for $m \leq n$. As with the single initiating neutron case, the equations are all coupled in sequence and thus it is necessary to first solve the single initiating neutron case up to $n = N$ and then begin to solve the intrinsic source case from $n = 0$ in sequence to $n = N$, where N is the highest order source number probability required. This process makes the equations for the source number probabilities even more lengthy than in the single initiating neutron case. Consequently, due to memory requirements, only equations up to $n = 45$ have been derived for the intrinsic source for a maximum fission multiplicity of $K_Q = 10$ in the course of writing this paper.

4. One-Dimensional Semi-Analytical Solutions in Slab Geometry

4.1. Steady State POI in a Slab Model

Before proceeding with the numerical solution of the space and time dependent number probability equations derived above, we present a semi-analytic solution based on quadratures for the steady state survival probability, or probability of initiation (POI), in a homogeneous supercritical system. In addition to having intrinsic value as an inexpensive method for computing the POI in 1D planar or slab geometry, the solution obtained by an independent method will provide confidence that the spatial discretisation method and iterative treatment of the nonlinear terms used in the numerical solution are acceptably accurate.

Setting the time-derivative in Eq.(26) to zero, the POI satisfies:

$$-D\frac{d^2p_s(x)}{dx^2} = \bar{\nu}\Sigma_f p_s(x) - \Sigma_a p_s(x) - \Sigma_f \sum_{k=2}^{K} \frac{(-1)^k \chi_k}{k!} p_s(x)^k, \quad -\frac{T}{2} \leq x \leq \frac{T}{2}, \quad (38)$$

where T is the slab thickness. To facilitate solution we replace the Marshak condition at the free surface by the Dirichlet boundary condition:

$$p_s(\pm\frac{T}{2}) = 0. \quad (39)$$

Dividing through by Σ_a and making the change of variable $y = x/L$, where L is the diffusion length given by $L = (D/\Sigma_a)^{1/2}$, Eq.(38) reduces to:

$$\begin{aligned} \frac{d^2p_s(y)}{dy^2} &= -\Big(\frac{\bar{\nu}\Sigma_f}{\Sigma_a} - 1\Big)p_s(y) + \frac{\Sigma_f}{\Sigma_a}\sum_{k=2}^{K}\frac{(-1)^k\chi_k}{k!}p_s(y)^k, \\ &= \Phi(p_s), \end{aligned} \quad (40)$$

which defines the nonlinear function $\Phi(p_s)$. This equation for p_s is autonomous, i.e., the independent variable y does not appear explicitly in the equation, and hence can be solved by first converting the second order equation to coupled first order equations for p_s and $Q \equiv dp_s/dy$, i.e. :

$$\frac{dQ}{dy} = \Phi(p_s), \quad (41a)$$

$$\frac{dp_s}{dy} = Q, \tag{41b}$$

Now dividing the two equations yields the single first order nonlinear equation:

$$Q\,\frac{dQ}{dp_s} = \Phi(p_s). \tag{42}$$

From the symmetry of the problem it follows that $p_s'(0) = Q(0) = 0$, which allows the solution of Eq.(42) to be expressed as:

$$\frac{Q^2}{2} = \int_{p_s(0)}^{p_s} \Phi(u)\,du. \tag{43}$$

From Eq.(40), $\Phi(u)$ is a polynomial which when inserted in Eq.(43) can be integrated to give, upon also recalling Eq.(41b) :

$$\frac{dp_s(y)}{dy} = -\sqrt{2\sum_{k=1}^{K}(-1)^k m_k\left[p_s^{k+1}(y) - p_s^{k+1}(0)\right]}, \tag{44}$$

where the negative square root has been chosen from physical considerations such that the solution is monotonically decaying from the centre of the slab to either boundary, and m_k is defined as:

$$\begin{aligned} m_k &= \frac{(k_\infty - 1)}{2} \quad k = 1, \\ &= \frac{\Sigma_f \chi_k}{\Sigma_a (k+1)!} \quad k \geq 2. \end{aligned} \tag{45}$$

Making the substitution $z = p_s(y)/p_s(0)$ in Eq.(44), the latter can be separated and integrated over the entire domain to yield:

$$\int_0^1 \frac{dz}{\sqrt{2\sum_{k=1}^{K}(-1)^k m_k p_s(0)^{k-1}\left[z^{k+1} - 1\right]}} = \frac{\tilde{T}}{2}, \tag{46}$$

where $\tilde{T} = T/L$ is the slab thickness in diffusion length units. Equation (46) represents a non-linear equation for $p_s(0)$, the value of the POI at the slab centre, and must be solved numerically. Expressing this equation as:

$$g(p_s(0)) = \int_0^1 \frac{dz}{\sqrt{2\sum_{k=1}^{K}(-1)^k m_k p_s(0)^{k-1}\left[z^{k+1} - 1\right]}} - \frac{\tilde{T}}{2} = 0, \tag{47}$$

the following Newton scheme can be used to iteratively find the root of the equation and hence the desired $p_s(0)$:

$$p_s^{(j+1)}(0) = p_s^{(j)}(0) - \frac{g\left(p_s^{(j)}(0)\right)}{g'\left(p_s^{(j)}(0)\right)}, \quad j = 0, 1, \cdots \tag{48}$$

where j is the iteration index and a starting value $p_s^{(0)}(0)$ is assumed. For a supercritical system, there is only one non-zero root in the interval $(0,1)$ while there are no non-zero roots for a subcritical or critical system (Bell, 1963, 1965; Pázsit and Pál, 2008). With the integrals in $g(p_s^{(j)}(0))$ and $g'(p_s^{(j)}(0))$ evaluated using an adaptive Gauss-Kronrod quadrature routine in MATLAB (2012), convergence is achieved with relatively few iterations.

The number of iterations required to converge the Newton iteration depends on the initial guess implemented in Eq.(48). Table (1) shows the number of iterations required for three different k_{eff} to converge based on a number of different starting points. No convergence is represented by '-'.

			iterations required for convergence from initial guess									
k_{eff}	p_s^{centre}	$\tilde{T}$	0.001	0.005	0.01	0.05	0.1	0.2	0.3	0.4	0.5	0.6
1.01	0.0088	2.2106	4	4	4	5	5	6	7	7	9	-
1.05	0.0421	2.2763	4	5	5	5	5	6	6	7	9	-
1.1	0.0803	2.3596	5	5	5	5	5	6	6	7	9	-

Table 1: Number of iterations required for the convergence of the Newton iteration following the use of a Gauss-Kronrod quadrature scheme implemented in MATLAB (2012).

Once the POI at the centre point has been obtained, it is possible to calculate the POI at other spatial points in the slab by integrating Eq.(44) over $[(0,y)\times(p_s(0),p_s(y))]$ and again using a Newton method to obtain $p_s(y)$ as a function of y. However, a more efficient approach is to solve Eq.(44) numerically using a standard method for nonlinear first order differential equations. We implemented a four point Runge-Kutta algorithm with the following steps. Rewriting Eq.(44) as:

$$\frac{dz(y)}{dy} = \sqrt{2\sum_{k=1}^{K}(-1)^k m_k(1-z^{k+1})p_s(0)^{k-1}} \equiv f(y,z). \tag{49}$$

the fourth order Runge-Kutta scheme starts from the boundary value and finds the next spatial point by using a trial step at the midpoint of a spatial interval to cancel out lower order error terms. The four point solution is constructed using

$$\begin{aligned} K_1 &= \Delta y f(y,z), \\ K_2 &= \Delta y f\Big(y+\frac{\Delta y}{2}, z+\frac{K_1}{2}\Big), \\ K_3 &= \Delta y f\Big(y+\frac{\Delta y}{2}, z+\frac{K_2}{2}\Big), \\ K_4 &= \Delta y f(y+\Delta y, z+K_3), \end{aligned} \tag{50}$$

and

$$z^{(i+1)} = z^{(i)} + \frac{K_1}{6} + \frac{K_2}{3} + \frac{K_3}{3} + \frac{K_4}{6}, \tag{51}$$

where i is the index for the spatial interval.

The solution obtained from the implementation of the Newton and Runge-Kutta methods is shown in figure 1 for three values of k_{eff} obtained by the variation in slab size for the given cross section and multiplicity data.

The cross section data used was created by investigating the fission spectrum of a system of 5.91% ^{240}Pu and 93.27% ^{239}Pu of density 19.098 gcm^{-3}, where the additional mass is made up of other isotopes of Pu, over the 172 group XMAS group structure. To obtain a fast spectrum, the energy limits were selected based on the energy at which over 90% of the total neutrons from fission were created. This gave an energy range of 4.076×10^5eV to 1.964×10^7eV which was then used in conjunction with WIMS (2014) to generate fast data for the system in a diffusion model with isotropic scattering, this can be seen in table (3). The multiplicity data for induced fission used was that given in table 1 of Enqvist et al. (2006), reproduced for convenience in table (2). These fission probabilities correspond to the system considered in Enqvist et al. (2006) of 80% ^{239}Pu and 20% ^{240}Pu. The neutron velocity used was $v = 2.85 \times 10^9 cms^{-1}$ corresponding to the fast group of the six group discretisation used in Hansen and Roach (1961).

Neutrons	0	1	2	3	4	5	6	7	8
$p_f(n)$	0.0071	0.0674	0.2283	0.3263	0.2510	0.0958	0.0208	0.0029	0.0005

Table 2: Induced fission probabilities, reproduced from Enqvist et al. (2006)

cross section (cm^{-1})	Σ_t	Σ_a	Σ_f
	3.7426×10^{-1}	8.8346×10^{-2}	8.5949×10^{-2}

Table 3: WIMS (2014) generated cross section data for fast neutrons in a diffusion model with isotropic scattering.

4.2. Approximate analytical solution for the centre values in the quadratic model

We conclude this section by providing an analytical approximation for the POI in the form of a series expansion. It has been shown that for weakly supercritical systems, so that the POI is small, sufficient accuracy can be achieved by truncating the nonlinear terms at second order, the so-called quadratic approximation (Bell, 1963). Under these conditions Eq.(47) simplifies to:

$$\frac{1}{\sqrt{2}} \int_0^1 \frac{dz}{\sqrt{m_1(1-z^2) - m_2 p_0 (1-z^3)}} = \frac{\tilde{T}}{2}, \tag{52}$$

which can be rearranged to give

$$\frac{1}{\sqrt{2m_1}} \int_0^1 \frac{dz}{\sqrt{1-z^2}} \left[1 - p_0 \frac{m_2(1-z^3)}{m_1(1-z^2)} \right]^{-\frac{1}{2}} = \frac{\tilde{T}}{2}. \tag{53}$$

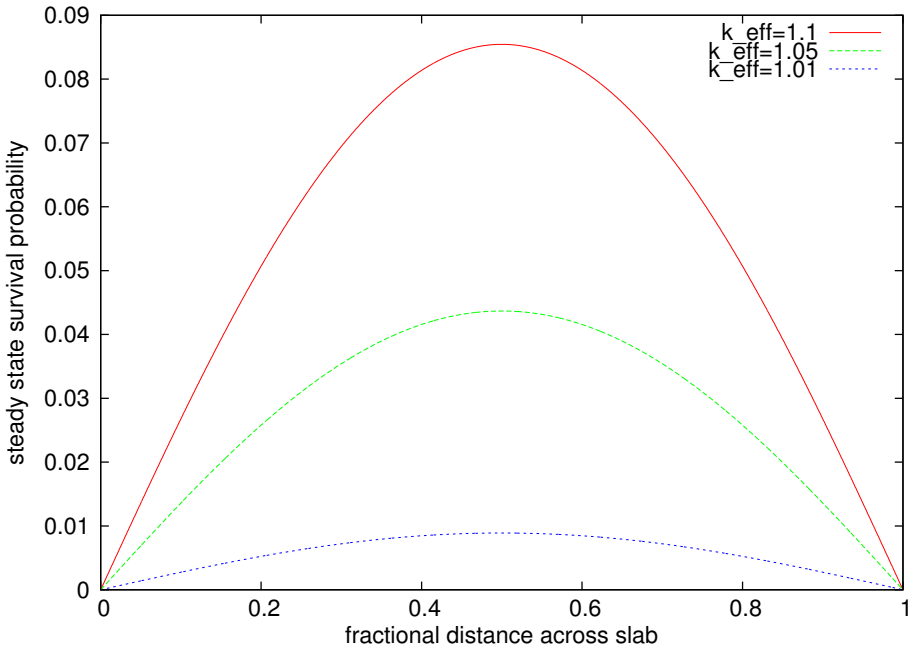


Figure 1: Steady state solutions of the survival probability in supercritical media for various values of k_{eff}.

For $p_0 \ll 1$, which holds when $k_{eff} - 1 \ll 1$, the square root can be expanded using a series expansion to get:

$$\frac{1}{\sqrt{2m_1}} \int_0^1 \frac{dz}{\sqrt{1-z^2}} \left[1 + \frac{m_2}{m_1} p_0 \left(\frac{1-z^3}{1-z^2} \right) + \frac{3}{8} \left(\frac{m_2}{m_1} \right)^2 p_0^2 \left(\frac{1-z^3}{1-z^2} \right)^2 + ... \right] = \frac{\tilde{T}}{2}. \quad (54)$$

Neglecting terms of orders higher than second in p_0 and performing the integrals yields the following quadratic equation for p_0:

$$I_2 p_0^2 + I_1 p_0 + \left(I_0 - \tilde{T}/2 \right) = 0, \quad (55)$$

where the coefficients are given by:

$$\begin{aligned} I_0 &= \frac{1}{\sqrt{2m_1}} \int_0^1 \frac{dz}{\sqrt{1-z^2}} = \frac{1}{\sqrt{2m_1}} \frac{\pi}{2} \\ I_1 &= \frac{1}{\sqrt{2m_1}} \frac{1}{2} \left(\frac{m_2}{m_1} \right) \int_0^1 dz \frac{(1-z^3)}{(1-z^2)^{3/2}} = \frac{1}{\sqrt{2m_1}} \left(\frac{m_2}{m_1} \right) \\ I_2 &= \frac{1}{\sqrt{2m_1}} \frac{3}{8} \left(\frac{m_2}{m_1} \right)^2 \int_0^1 dz \frac{(1-z^3)^2}{(1-z^2)^{5/2}} = \frac{1}{\sqrt{2m_1}} \frac{3}{8} \left(\frac{m_2}{m_1} \right)^2 \left[\frac{5\pi}{4} - \frac{4}{3} \right] \end{aligned} \quad (56)$$

The physically interesting solution is given by the positive root:

$$p_0 = \frac{1}{2} \left[\sqrt{\left(\frac{I_1}{I_2} \right)^2 + \frac{4}{I_2} \left(\frac{\tilde{T}}{2} - I_0 \right)} - \frac{I_1}{I_2} \right] \quad (57)$$

Additionally, it is interesting to see how the centre value will change for different numbers of retained terms in Eq.(54). For terms retained up to orders three, four and five, Eq.(55) becomes Eqs.(58a), (58b) and (58c) respectively

$$I_3 p_0^3 + I_2 p_0^2 + I_1 p_0 + \left(I_0 - \tilde{T}/2\right) = 0 \tag{58a}$$

$$I_4 p_0^4 + I_3 p_0^3 + I_2 p_0^2 + I_1 p_0 + \left(I_0 - \tilde{T}/2\right) = 0 \tag{58b}$$

$$I_5 p_0^5 + I_4 p_0^4 + I_3 p_0^3 + I_2 p_0^2 + I_1 p_0 + \left(I_0 - \tilde{T}/2\right) = 0 \tag{58c}$$

where I_2, I_1 and I_0 are as given in Eq.(56) and additionally

$$\begin{aligned}
I_3 &= \frac{1}{\sqrt{2m_1}}\frac{5}{16}\left(\frac{m_2}{m_1}\right)^3 \int_0^1 dz \frac{(1-z^3)^3}{(1-z^2)^{7/2}} = \frac{1}{\sqrt{2m_1}}\frac{5}{16}\left(\frac{m_2}{m_1}\right)^3 \times 3.42094 \\
I_4 &= \frac{1}{\sqrt{2m_1}}\frac{35}{128}\left(\frac{m_2}{m_1}\right)^4 \int_0^1 dz \frac{(1-z^3)^4}{(1-z^2)^{9/2}} = \frac{1}{\sqrt{2m_1}}\frac{35}{128}\left(\frac{m_2}{m_1}\right)^4 \times 4.58146 \\
I_5 &= \frac{1}{\sqrt{2m_1}}\frac{63}{256}\left(\frac{m_2}{m_1}\right)^5 \int_0^1 dz \frac{(1-z^3)^5}{(1-z^2)^{11/2}} = \frac{1}{\sqrt{2m_1}}\frac{63}{256}\left(\frac{m_2}{m_1}\right)^5 \times 6.21897
\end{aligned} \tag{59}$$

The solutions to Eqs.(58a), (58b) and (58c) were solved using a Newton-Raphson iterative scheme to obtain the values of the appropriate root of these equations. The results for the centre value in the quadratic model are shown for different numbers of retained terms in the series expansion in table (4).

k_{eff}	2 terms	3 terms	4 terms	5 terms	Gauss-Kronrod
1.01	8.7660×10^{-3}	8.7648×10^{-3}	8.7648×10^{-3}	8.7648×10^{-3}	8.7648×10^{-3}
1.005	4.4048×10^{-3}	4.4047×10^{-3}	4.4047×10^{-3}	4.4047×10^{-3}	4.4047×10^{-3}
1.001	8.8457×10^{-4}	8.8456×10^{-4}	8.8456×10^{-4}	8.8456×10^{-4}	8.8460×10^{-4}

Table 4: Comparison between different number of retained terms in the series expansion in Eq.(54) and Gauss-Kronrod method for different values of k_{eff}.

As shown in table (4), the above approximate analytical result for the centre value of the POI in the quadratic approximation is very accurate when compared to the numerically exact result obtained in Section 4.1 using Gauss-Kronrod quadrature. Whilst an increase in accuracy is seen for a greater number of retained terms, this is not further improved beyond retaining three terms in the series expansion.

5. Numerical Solutions in a Slab Geometry

We consider now the numerical solution of the coupled system of equations for the number probabilities. We begin by developing and testing the numerical scheme in slab geometry containing a homogeneous subcritical mixture of ^{239}Pu and ^{240}Pu, thereby

giving a uniformly distributed spontaneous fission source, and obtain the neutron survival probability in the slab as well as the probability of finding a given number of neutrons in the entire slab.

5.1. Single Initiating Neutron

In 1D slab geometry, the equation for the survival probability reads:

$$\frac{1}{v}\frac{\partial p_s(x,s)}{\partial s} - D\frac{\partial^2 p_s(x,s)}{\partial x^2} = \bar{\nu}\Sigma_f p_s(x,s) - \Sigma_a p_s(x,s) - \Sigma_f \sum_{k=2}^{K} \frac{(-1)^k \chi_k}{k!} p_s(x,s)^k, \quad (60)$$

with initial condition:

$$p_s(x,0) = \mathcal{I}_R(x), \quad (61)$$

that gives the neutron survival probability for the entire slab, and the homogeneous Dirichlet boundary conditions:

$$\begin{aligned} p_s(0,s) &= 0 \\ p_s(T,s) &= 0 \end{aligned} \quad (62)$$

where T is the slab thickness. We use a simple boundary condition here so the numerical solution can be benchmarked against the semi-analytical solution obtained previously for this boundary condition, but revert to the more accurate Marshak condition in the more interesting spherical geometry case.

The spatial domain $[0, T]$ is discretised using a mesh of $I + 1$ evenly spaced points x_i, $i = 0, 1, 2, \ldots, I$, such that $x_0 = 0, x_1 = x_0 + \Delta x, \ldots, x_i = x_{i-1} + \Delta x, \ldots, x_I = T$, where $\Delta x = T/I$ is the cell width, and the second order spatial derivative is then discretised on this mesh using central differences. Similarly, a time discretisation is introduced over the time interval $[0, s_{max}]$ with constant time step Δs and the equations are evolved in time with a Crank-Nicholson method. This scheme yields second order accuracy in space and time for all number probabilities of order greater than or equal to one, as these satisfy linear equations. The survival probability equation is nonlinear and requires iterative relaxation of the nonlinear terms at every time step. Although Newton linearisation is readily implemented at each time step, we have found that a simpler linearisation combined with Picard iteration yields rapid convergence, for the application of interest here. Specifically, the nonlinear terms are factored and rearranged such that at iteration level r the equation for the survival probability, Eq.(60) becomes:

$$\frac{1}{v}\frac{\partial p_s^{(r)}(x,s)}{\partial s} = D\frac{\partial^2 p_s^{(r)}(x,s)}{\partial x^2} + (\bar{\nu}\Sigma_f - \Sigma_a) p_s^{(r)}(x,s) - \Sigma_f \sum_{k=2}^{K} \frac{(-1)^k \chi_k}{k!} \left[p_s^{(r-1)}(x,s)\right]^{k-1} p_s^{(r)}(x,s). \quad (63)$$

The discretised system can then be expressed as:

$$H^-(s + \Delta s) p_s^{(r)}(s + \Delta s) = H^+(s) p_s^{(r)}(s), \quad r = 1, 2, \ldots, \quad (64)$$

where H^- and H^+ are $(I+1)\times(I+1)$ tri-diagonal matrix with subdiagonal, diagonal and superdiagonal elements given by, respectively:

$$
\begin{aligned}
H^-_{subdiag} &= -\frac{1}{4}\frac{D_{i-1}+D_i}{(\Delta x)^2} \\
H^-_{diag} &= \frac{1}{\Delta s\ \ v} + \frac{1}{4}\frac{D_{i-1}+2D_i+D_{i+1}}{(\Delta x)^2} - \frac{1}{2}\bar{\nu}\Sigma_f + \frac{1}{2}\Sigma_a - \frac{1}{2}\Sigma_f \sum_{k=2}^{K} \frac{(-1)^k \chi_k}{k!} \left[p_s^{(r-1)}(x_i, s+\Delta s)\right]^{k-1} \\
H^-_{superdiag} &= -\frac{1}{4}\frac{D_i+D_{i+1}}{(\Delta x)^2}
\end{aligned}
\tag{65}
$$

$$
\begin{aligned}
H^+_{subdiag} &= \frac{1}{4}\frac{D_{i-1}+D_i}{(\Delta x)^2} \\
H^+_{diag} &= \frac{1}{\Delta s\ \ v} - \frac{1}{4}\frac{D_{i-1}+2D_i+D_{i+1}}{(\Delta x)^2} + \frac{1}{2}\bar{\nu}\Sigma_f - \frac{1}{2}\Sigma_a + \frac{1}{2}\Sigma_f \sum_{k=2}^{K} \frac{(-1)^k \chi_k}{k!} \left[p_s^{(\infty)}(x_i, s)\right]^{k-1} \\
H^+_{superdiag} &= \frac{1}{4}\frac{D_i+D_{i+1}}{(\Delta x)^2}
\end{aligned}
\tag{66}
$$

The solution proceeds by introducing an initial guess $p_s^{(0)}$ to evaluate the H^- matrix, which, after the first time step, is just taken to be the converged value $p_s^{(\infty)}$ at the previous timestep. The H^- matrix is then inverted to obtain an updated solution, and the process iterated until convergence is achieved. The solution is then advanced in time over successive time steps to the final time.

To assess the convergence of the scheme, we consider the time evolution of the survival probability for the central node as shown in figure 2 for cross sections as given in table (3), induced fission probabilities as given in table (2) and for a timestep of $\Delta s = 1\times 10^{-12}$s.

The number of iterations to converge the nonlinearity to machine precision at various times within the time evolution of the survival probability is shown in table (5). As can be seen, relatively few iterations were required for a converged solution. The exact numbers vary depending on the time step and time into the simulation but it is clear that roughly 5 iterations suffice to achieve convergence to machine precision.

Once the survival probability was calculated, the number probabilities were derived by considering the differentials of the slab geometry version of Eq.(21) with respect to z, as described in Section 3. These equations are linear, however the differentiations introduce an additional inhomogeneous term, as a sum of the products of previously calculated number probabilities, which can be treated as a "source-like" term and will be referred to as N. This modifies Eq.(64) as

$$H^-(s+\Delta s)p_n(s+\Delta s) = H^+(s)p_n(s) + N, \tag{67}$$

with initial condition:

$$p_n(x,0) = \delta_{n,1}\mathcal{I}_R, \tag{68}$$

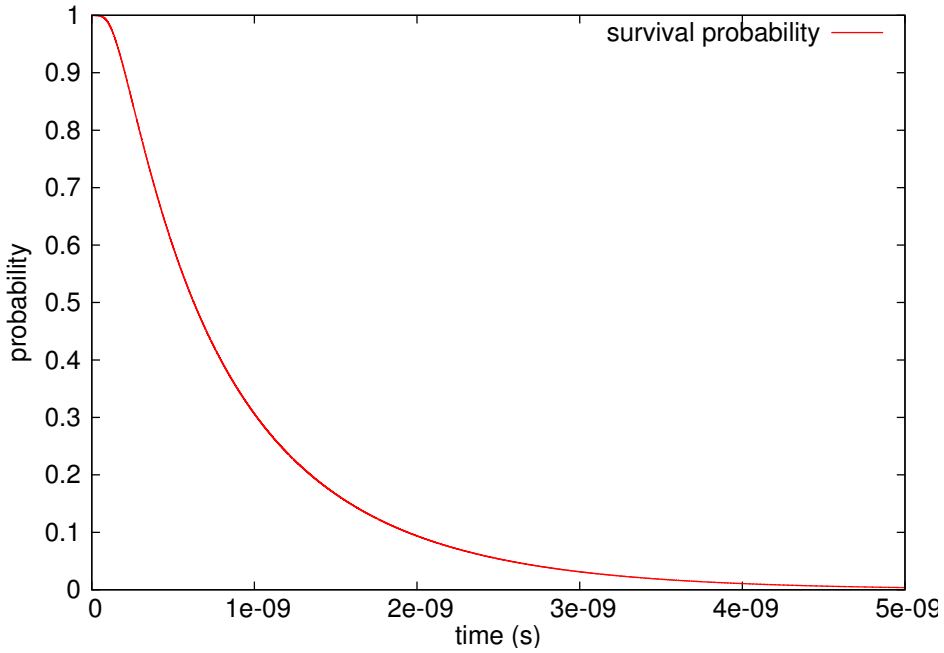


Figure 2: Time evolution of the survival probability at the central node in a slab geometry.

	iterations required for convergence at time (s)						
Δs	0	1×10^{-9}	2×10^{-9}	3×10^{-9}	4×10^{-9}	5×10^{-9}	p_s at 5×10^{-9}
5×10^{-13}	5	5	5	4	4	4	3.759×10^{-3}
1×10^{-12}	5	5	5	4	4	4	3.761×10^{-3}
5×10^{-12}	6	6	6	5	5	4	3.777×10^{-3}
1×10^{-11}	6	6	6	5	5	4	3.797×10^{-3}
5×10^{-11}	8	8	7	6	6	5	3.954×10^{-3}

Table 5: Number of iterations required for the convergence to machine precision of iterative scheme for non-linear survival probability in slab geometry for a suitable CFL number to avoid oscillations at the boundaries

and boundary conditions:

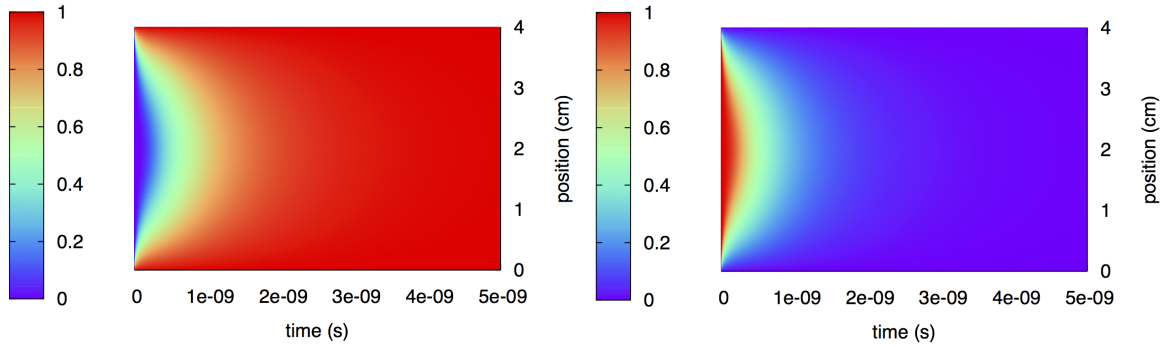
$$\begin{aligned} p_n(0,s) &= 0, \\ p_n(T,s) &= 0. \end{aligned} \tag{69}$$

As Eq.(67) is linear in $p_n(x,s)$, the need for an iterative process is removed and consequently the matrix H is given by

$$
\begin{aligned}
H^{-}_{subdiagonal} &= -\frac{1}{4}\frac{D_{i-1}+D_i}{(\Delta x)^2} \\
H^{-}_{diagonal} &= \frac{1}{\Delta s \quad v} + \frac{1}{4}\frac{D_{i-1}+2D_i+D_{i+1}}{(\Delta x)^2} - \frac{1}{2}\bar{\nu}\Sigma_f + \frac{1}{2}\Sigma_a - \frac{1}{2}\Sigma_f \sum_{k=2}^{K} \frac{(-1)^k \chi_k}{(k-1)!} p_s^{k-1} \\
H^{-}_{superdiagonal} &= -\frac{1}{4}\frac{D_i+D_{i+1}}{(\Delta x)^2}
\end{aligned}
\tag{70}
$$

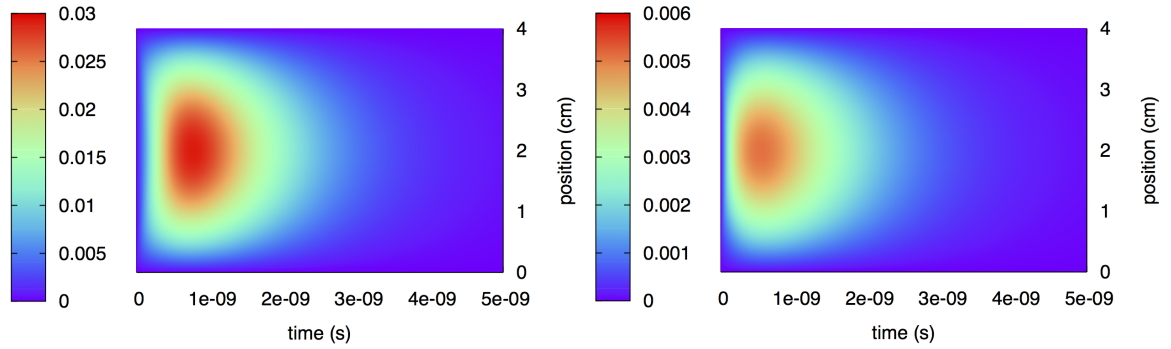
The equations, as described above, have been solved for probabilities of induced fission from table (2) for a 5.91% ^{240}Pu and 93.27% ^{239}Pu system, taken from Enqvist et al. (2006) and cross sections as shown in table (3).

Numerical results for various number probabilities are shown in figures 3a, 3b, 4a, 4b, 5a and 5b.



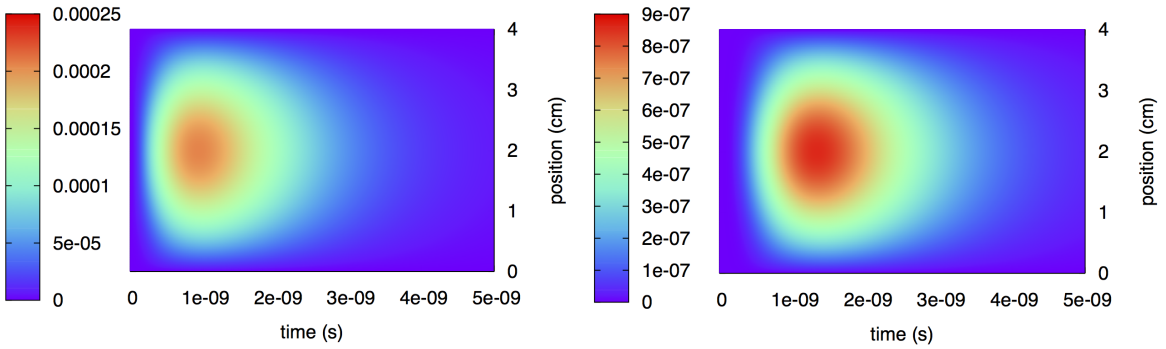
(a) p_0 (b) p_1

Figure 3: Number probabilities in a one-dimensional slab with $k_{eff} = 0.423$ for p_0 and p_1.



(a) p_2 (b) p_5

Figure 4: Number probabilities in a one-dimensional slab with $k_{eff} = 0.423$ for p_2 and p_5.



(a) p_{10} (b) p_{20}

Figure 5: Number probabilities in a one-dimensional slab with $k_{eff} = 0.423$ for p_{10} and p_{20}.

Whilst neutron number probability distributions up to order 50 can be computed with the current algorithm, the probabilities drop off substantially with increasing neutron number. Table (6) shows the maximum value of the neutron number probability distributions over the time and space ranges investigated. As can be seen from this table, over 99% of the neutrons within the system are accounted for within the first five number probabilities.

Neutrons	Maximum probability distribution value	Minimum sum of probability value
5	5.2769×10^{-3}	0.99440
10	2.2067×10^{-4}	0.99957
15	1.3758×10^{-5}	0.99984
20	9.8869×10^{-7}	0.99986

Table 6: Variation in maximum value of number distributions and minimum value cumulative probability distributions over the time and space range for 80 spatial intervals.

5.1.1. Benchmark of POI

For benchmark purposes, distributions for the POI obtained using the code in Section 5.1 were compared to the results derived in Section 4.1, for various values of k_{eff} in the supercritical regime. Figure 6 shows the fractional differences between the model developed in Section 5.1 and the benchmark developed in this section.

As can be seen from figure 6, good agreement is seen between the data established from the new model and from the benchmark with all differences being less than 0.003%. This indicates that our iterative treatment of the nonlinear terms is robust and that the spatial discretisation is accurate.

6. Numerical Results in Spherical Geometry

We now generalise the slab model developed to 1D spherical geometry but allow for multilayers and consider the survival and number probabilities in subregions of

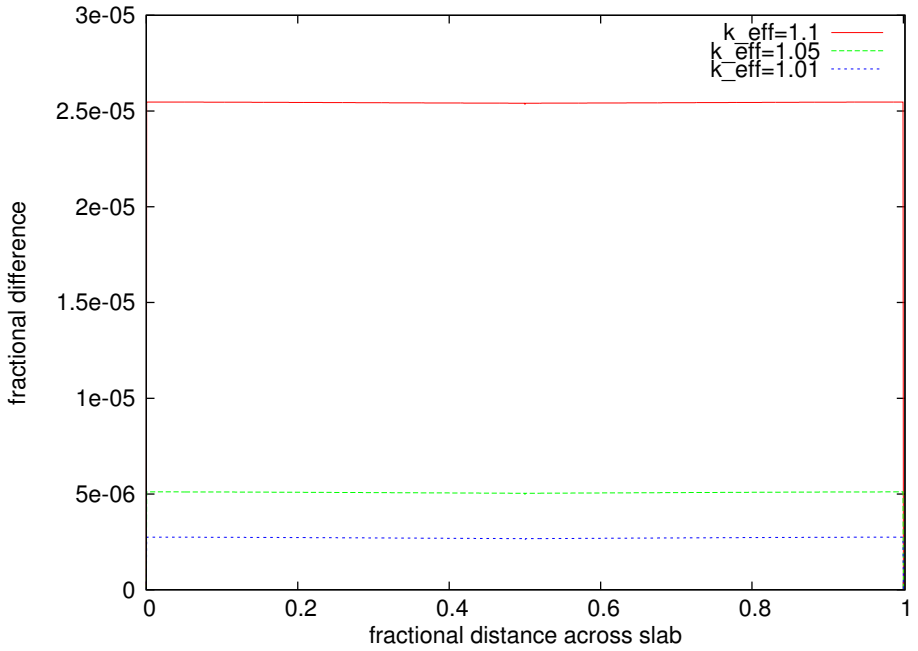


Figure 6: Fractional difference between code developed in Section 5.1 and the benchmark developed in Section 4.1 for different values of k_{eff}.

the system. We note that for the case of a single initiating neutron, the probabilities decay in time but depend on space through the location of the initial neutron. For the source case, the probabilities approach a steady state without any fine spatial structure because of the assumed homogeneity of the source region.

6.1. Homogenous Sphere: Single Initiating Neutron

Consider a sphere of radius r_B in which the material and source properties are uniform in the polar and azimuthal coordinates but are allowed to vary radially in a piecewise smooth manner. In this spherically symmetric system, the number probabilities then depend only on the radial position r of the initial neutron, that is, they are independent of where the neutron is located on a spherical surface at a fixed r. Equation (21) with $z = 0$ then reduces to the following for the survival probability:

$$\frac{1}{v}\frac{\partial p_s(r,s)}{\partial s} - \frac{1}{r^2}\frac{\partial}{\partial r}\left[Dr^2\frac{\partial p_s(r,s)}{\partial r}\right] = \bar{\nu}\Sigma_f p_s(r,s) - \Sigma_a p_s(r,s) - \Sigma_f \sum_{k=2}^{K} \frac{(-1)^k \chi_k}{k!} p_s(r,s)^k \tag{71}$$

with the initial condition

$$p_s(r,0) = \mathcal{I}_R(r), \tag{72}$$

where the subregion R is a spherical shell with radial bounds $r_{min} \leq r \leq r_{max}$, and where $r_{min} \geq 0$ and $r_{max} \leq r_B$. The boundary conditions are expressed as:

$$p_n(r_B,s) = -\frac{0.7104}{\Sigma_t}\frac{\partial p_n(r,s)}{\partial r}\bigg|_{r_B},$$
$$r^2\,\frac{\partial p_n(r,s)}{\partial r}\bigg|_{r=0} = 0, \tag{73}$$

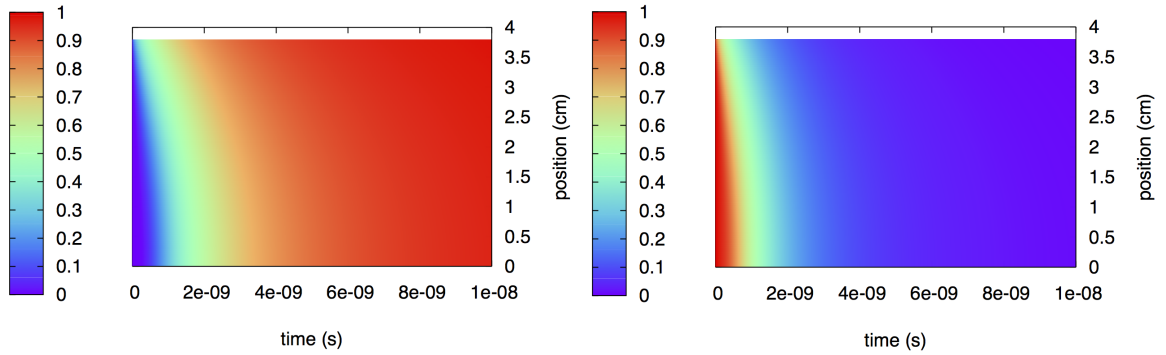
where we have now used the Marshak free surface condition at the $r = r_B$.

The numerical solution for the spherical case proceeds exactly as for the slab, with the linearised equation central-differenced in space, the nonlinearity iterated to convergence at each time step, and the solution advanced in time using Crank-Nicholson. We do not present the discretised system here, as it is similar to the slab system, but note that the Marshak boundary condition requires a first-order closure at the sphere boundary. As with the slab case, relatively few iterations are required to converge the nonlinear terms to machine precision. We note here that the k-eigenvalue quoted in the numerical results is computed using the same spatial discretisation and end-point corrected Marshak boundary condition as is used in the solution of the number probability equations. That is, the stated k_{eff} is consistent with the numerical scheme used in the paper.

The source terms in the equations for $p_n(r,s), n = 1, 2, \ldots$, arising from successive differentiations of the nonlinear terms with respect to the generating function variable z followed by setting $z = 0$, are identical in form to the slab case and thus no additional effort is necessary in developing these terms for the sphere case. In fact, as is obvious from the general equation, this is true for arbitrary geometry in any number of spatial dimensions. That is, once the derivatives have been expressed in terms of the number probabilities of the desired order, the terms arising from neutron branching are determined once and for all, which is an attractive attribute of the backward formulation. Again, the numerical solution of the equations for $p_n(r,s), n = 1, 2, \ldots$ proceeds as before, with respect to discretisation and time evolution, so we do not present further detail.
For the following results we model a bare plutonium sphere of radius 3.7938cm, with a k_{eff} of 0.7857. The cross sections used are as given in table 3 and the multiplicities are those calculated from the induced fission probabilities in table 2. Whilst the k_{eff} of this system is much larger than that of the slab considered previously, we note that the calculation of the first ten probabilities account for in excess of 99% of the neutrons in the system.

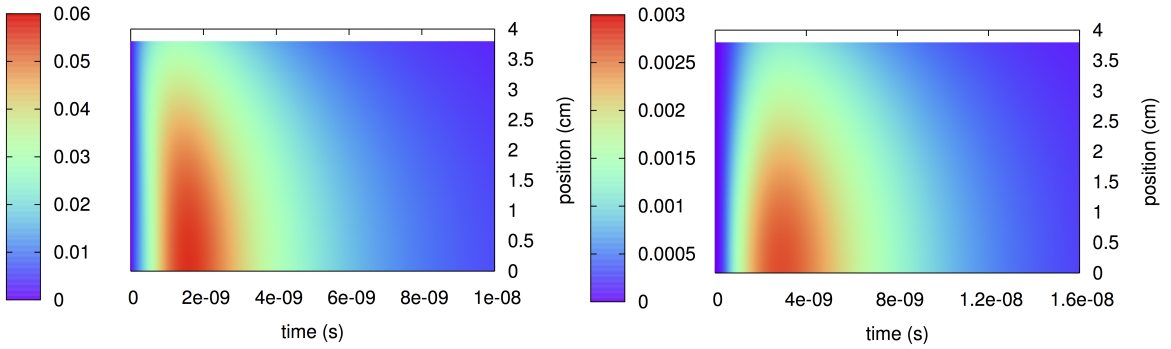
6.1.1. Number Probability in Entire Sphere

We consider first the region of interest to be the entire sphere: $r_{min} = 0$, $r_{max} = r_B$. That is, we are interested in the neutron number probabilities in the whole sphere with the initiating neutron injected anywhere on a spherical surface at a radial position r. Numerical results for different injection points and final times are shown in figures 7a, 7b, 8a and 8b



(a) p_0 (b) p_1

Figure 7: Number probabilities in the whole of a one-dimensional sphere with $k_{eff} = 0.7857$ for p_0 and p_1.



(a) p_2 (b) p_{10}

Figure 8: Number probabilities in the whole of a one-dimensional sphere with $k_{eff} = 0.7857$ for p_2 and p_{10}.

Consider first the graph shown in figure 7a showing the extinction probability in the whole sphere. The value for the extinction probability is initially 0, which is consistent with the initial condition. As time progresses, the extinction probability increases - due to either leakage from the system or absorption in the medium, causing a loss in neutrons. The closer the neutron is injected to the centre of the sphere, the longer it takes for the extinction probability to reach one. This due to the fact it is more likely to undergo fissions and is less likely to leak from the system as it has further to travel to the boundary of the sphere. As is expected from a sub-critical system as time increases the extinction probability tends to one.

The behaviour of $p_1(r, s)$ shown in figure 7b is opposite to that of the extinction probability. Initially $p_1(r, s)$ is one as the initiating neutron is injected on a spherical shell at every radius within the system, this decays with increasing time as neutrons may undergo fission, creating more neutrons; undergo absorption, removing neutrons or leaking from the system. Similarly to that of the extinction probability, the decay is delayed towards the centre of the sphere as the neutrons injected are less likely to

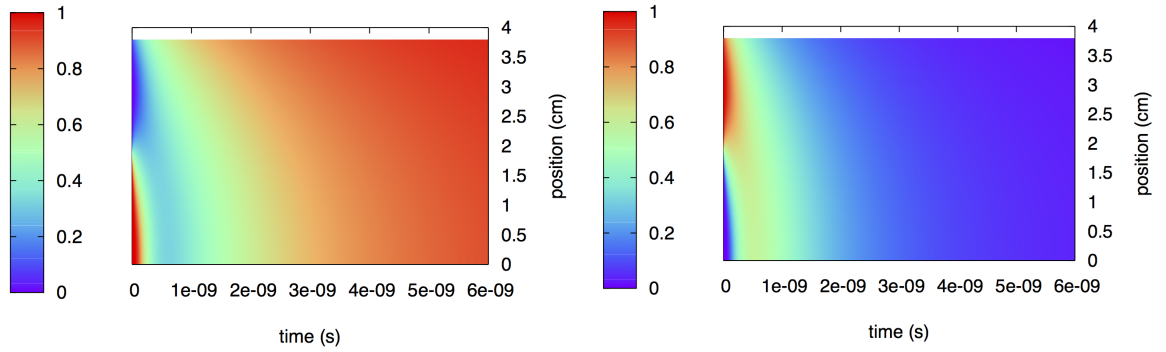
leak at early times as they would have to diffuse to the boundary to do so. A final point to note is that whilst the results show approximately the opposite behaviour to the extinction probability, the curve for $p_1(r, s)$ fits within the curve for the extinction probability. This is in line with expectation, as states with higher n are possible and so these cannot add to one on their own.

Figures 8a and 8b show similar behaviours. Both start at zero, as one neutron is initially injected on a spherical shell corresponding to each radius point. They both increase with time, due to the probability of fission events taking place within the medium and both show higher probabilities towards the centre where the injected neutrons are less likely to leak from the system and thus more likely to undergo fission. However, there are some important differences: firstly the magnitude of the two are different - showing we are much more likely to find two neutrons in the system than ten, this is in line with physical intuition for the very subcritical systems considered. Secondly, note the different scales of time for the two graphs - the probability for finding ten neutrons in the system is much more spread out in time than that of two neutrons: this is in line with expectation as it will take longer to build up ten neutrons in the system from fission events than two. This is also echoed in the wider near-zero strip at the beginning of figure 8b when compared to figure 8a - as the maximum fission multiplicity is eight, there cannot physically be ten neutrons in the system in the first time step and is unlikely at subsequent early timesteps. Finally, note the more strongly peaked distribution in figure 8b which describes the initial neutron needing to be injected closer to the centre of the system to produce ten neutrons. Again, this is due to increased likelihood of leakage the closer it is to the sphere's boundary and along with the longer times required to build up ten neutrons within the system, describes this behaviour.

It is observed that the time scale of the evolution of the number probabilities is faster than that predicted by the neutron lifetime, $1/(v\Sigma_a)$, of an infinite system. This is not surprising since we are concerned with a finite system with significant leakage, making the effective lifetime much smaller. Moreover, the reduction in the lifetime is amplified by the non-linear term in the equation for the survival probability, which acts to effectively increase the absorption in the system, and this effect propagates through the coupled equations describing the number probabilities of different orders. Thus, the overall effect is to make the time progression of the number probabilities faster than that predicted from simple intuitive estimates.

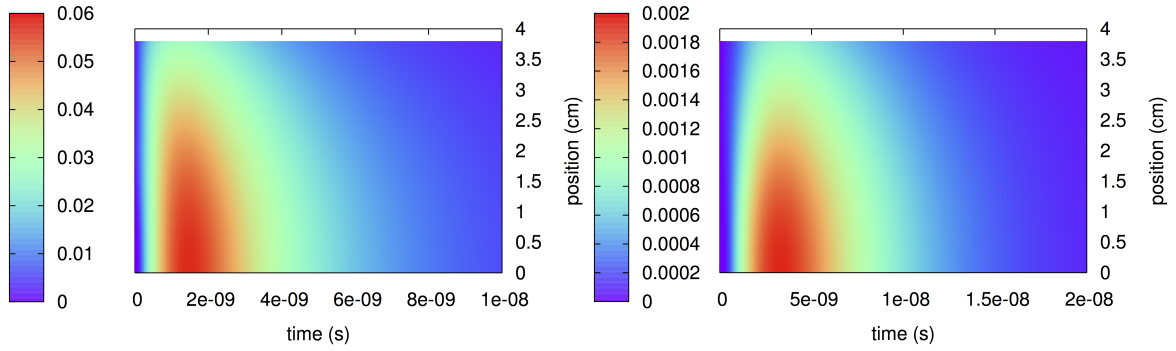
6.1.2. Number Probability in Outer Spherical Shell

The behaviour seen in the results for the probability of finding n neutrons in a spherical shell defined by $r_{min} = r_B/2, r_{max} = r_B$, i.e., a radial shell corresponding to the outer half of the sphere, show similar general behaviours to that of the results in the case of the whole sphere. With the extinction probability, shown in figure 9a, the two distinct regions at early times indicate the initial condition imposed - the probability is initially zero when the neutron is injected in the counting region and initially one when it is not. As time increases the probability for the neutrons injected in the counting region increases in the same manner as it did for figure 7a. In the region in which the neutrons were injected and not counted the probability drops from one as the one



(a) p_0 (b) p_1

Figure 9: Number probabilities in the outer half of a one-dimensional sphere with $k_{eff} = 0.7857$ for p_0 and p_1.



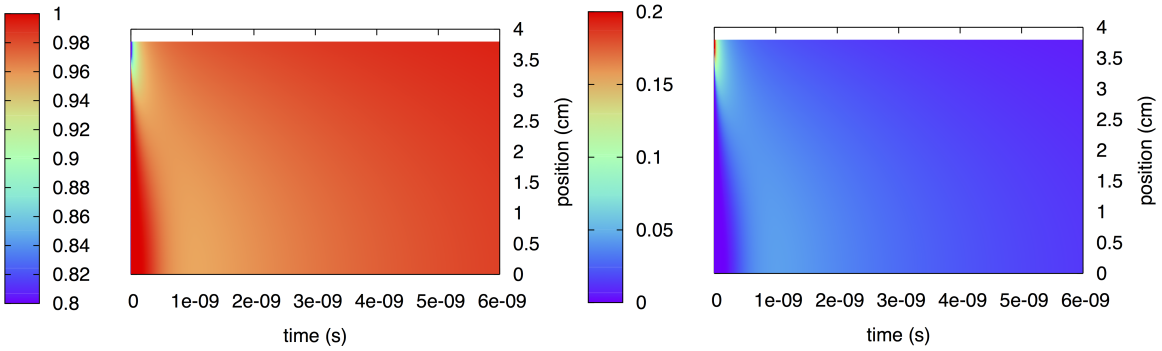
(a) p_2 (b) p_{10}

Figure 10: Number probabilities in the outer half of a one-dimensional sphere with $k_{eff} = 0.7857$ for p_2 and p_{10}.

neutron injected in the non-counting region diffuses over to the counting region - this takes longer the closer to the centre the initial neutron is injected, showing the curved shadow in the centre half of the sphere. Finally both regions then increase to one in line with expectation of the very subcritical systems being investigated.
Figure 9b shows complimentary behaviour to that of figure 9a, again we can note that the behaviour is somewhat compressed in time by comparison, allowing for other non-zero states. Finally, figure 10b shows similar behaviour to that shown in figure 8b, however it is important to note that the magnitude of figure 10b is smaller - this is likely to be due to the smaller counting region, as only the neutrons in the outer half are being counted, as opposed to the whole sphere.

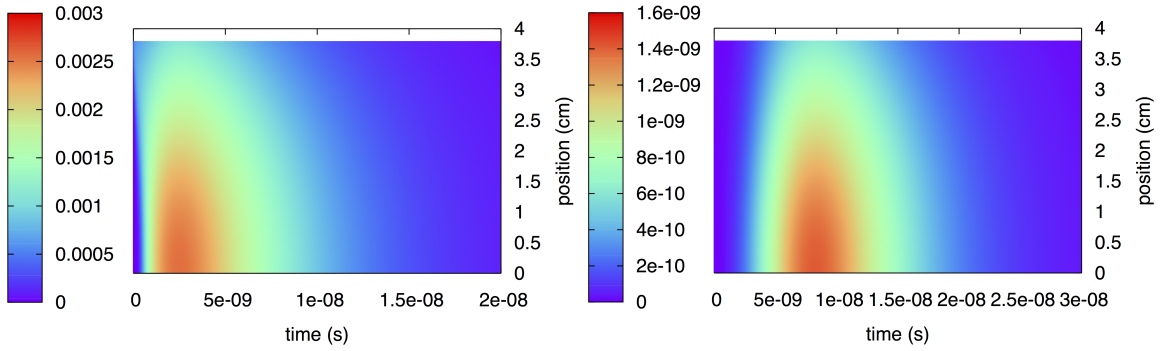
6.1.3. Number Probability in a Small Spherical Shell at the Boundary

Finally, we consider counting the neutrons in a small spherical shell on the boundary, of width equal to the boundary cell on the spherical mesh. Consider figure 11a: initially the extinction probability is zero everywhere, except for the edge of the sphere



(a) p_0 (b) p_1

Figure 11: Number probabilities in the boundary cell of a one-dimensional sphere with $k_{eff} = 0.7857$ for p_0 and p_1.



(a) p_2 (b) p_{10}

Figure 12: Number probabilities in the boundary cell of a one-dimensional sphere with $k_{eff} = 0.7857$ for p_2 and p_{10}.

- this is because there is zero probability of detecting no neutrons in the boundary cell if the neutron is initially injected into the boundary shell itself. As expected the probability of detecting no neutrons in this cell rapidly increases due to leakage. The converse of this is true for the probability of finding one neutron as shown in figure 11b. Both figures 11a and 11b show a curved shadow towards the centre region, this is for increasing probability in the case of $p_1(r, s)$ and for decreasing probability in the case of $p_0(r, s)$. This is due to the neutrons injected towards the centre taking a longer time to diffuse over to the region in which the neutrons are being counted and is a much more subtle example of the behaviour seen in figures 9a and 9b.

Figures 12a and 12b show very similar behaviours to the figures for $p_2(r, s)$ and $p_{10}(r, s)$ shown previously. Again, as the counting region is smaller, the probabilities are again much smaller here than in their larger counting region counterparts. It is possible to see an additional feature in figure 12a, namely the curved near-zero region at early times, which describes a higher likelihood of detecting two neutrons in the boundary

cell at early times if the initial neutron is injected nearer to the boundary cell itself.

6.2. Homogenous Sphere: Random Intrinsic Source

We now extend the numerical solutions for the single initiating neutron case to consider the distribution in the presence of a spatially uniform source in a homogeneous sphere. In light of this Eq.(14a), evaluated at $z = 0$ becomes

$$\frac{\partial\theta_0(s)}{\partial s} = Q\left[\sum_{k=1}^{K_Q}\frac{(-1)^k}{k!}\chi_k^{(Q)}\int_{r=0}^{r_B}4\pi r^2 dr\frac{3}{4\pi r_B^3}p_s^k(r,s)\right]\theta_0(s) \tag{74}$$

subject to the initial condition

$$\theta_0(0) = 1 \tag{75}$$

As $p_s(r,s)$ is present in this equation, the solution of Eq.(74) requires the solution of the single initiating neutron case, as described previously. Once the single initiating neutron case has been solved, the solution of Eq.(74) proceeds simply through its discretisation, as shown in Eq.(76) and a Crank-Nicholson scheme in time.

$$\frac{\partial\theta_0(s)}{\partial s} = \frac{3Q}{R^3}\left[\sum_{k=1}^{K_Q}\frac{(-1)^k}{k!}\chi_k^{(Q)}\sum_{i=1}^{I}r_i^2 p_s^k(r_i,s)\right]\theta_0(s) \tag{76}$$

As with the single initiating neutron case, individual source number probabilities can be extracted by taking derivatives of Eq.(74) with respect to z and then setting $z = 0$ in the resulting equation to give $\theta_n(s)$, as demonstrated in Section 3. This section also shows the dependence of $\theta_n(s)$ on $p_n(r,s)$, illustrating the need for the full solution of the single initiating neutron case before the source case can be calculated. The individual source number probabilities, $\theta_n(s)$ are then subject to the initial condition

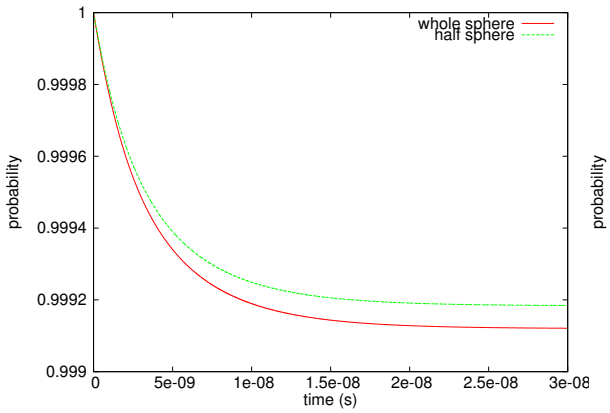
$$\theta_n(0) = 0 \tag{77}$$

As the source is spatially uniform, the distributions for $\theta_n(s)$ are also uniform in space, the results for the three counting regions can be seen in figures 13a, 13b, 14a, 14b, 15a, 15b, 16a and 16b. The source multiplicities are calculated from the spontaneous fission probabilities as given in Enqvist et al. (2006) which are replicated in table (7) for convenience. Again these fission probabilities correspond to a system of 80% ^{239}Pu and 20% ^{240}Pu, as is considered in Enqvist et al. (2006).

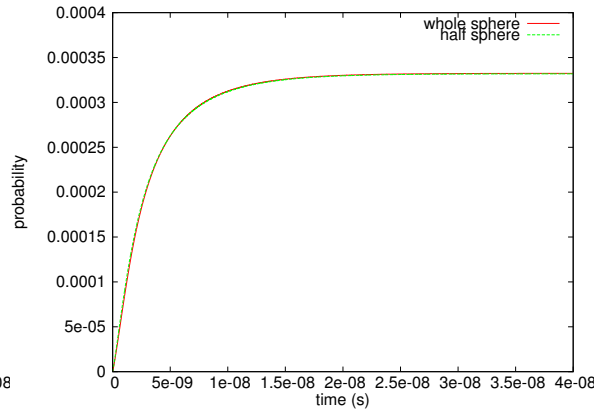
Neutrons	0	1	2	3	4	5	6
$p_f^{(s)}(n)$	0.0638	0.2316	0.3325	0.2533	0.0987	0.0181	0.0020

Table 7: Spontaneous fission probabilities, reproduced from Enqvist et al. (2006)

Figure 13a shows the comparison of the extinction probability for the half-sphere region and the full sphere region. As would be expected we see that the extinction probability

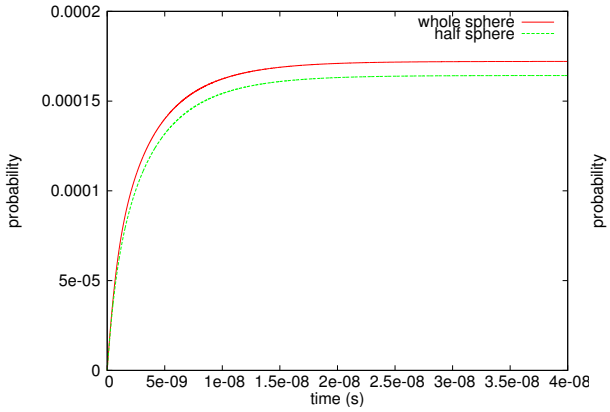


(a) θ_0

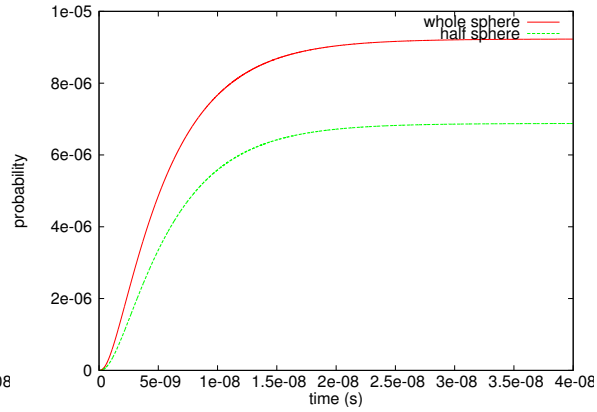


(b) θ_1

Figure 13: Comparison of source number probabilities for a whole sphere and outer half spherical shell of a one-dimensional sphere with $k_{eff} = 0.7857$ for θ_0 and θ_1.



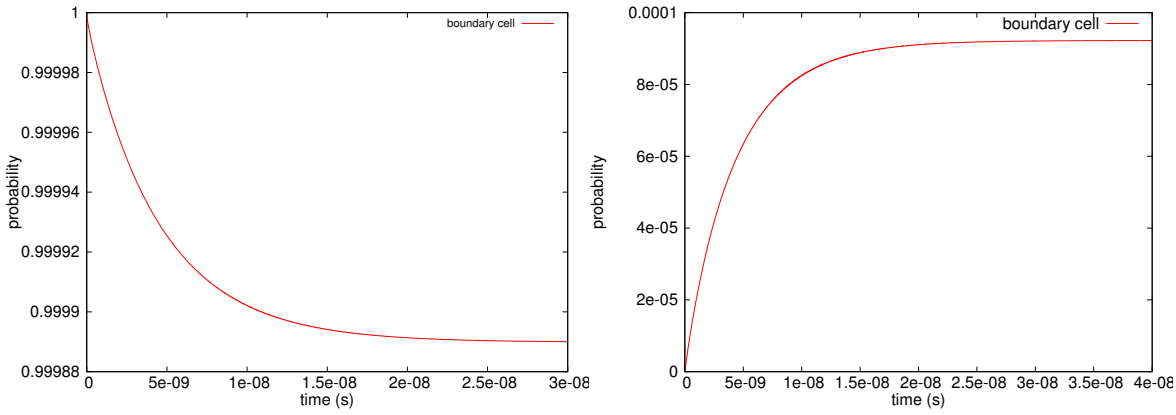
(a) θ_2



(b) θ_{10}

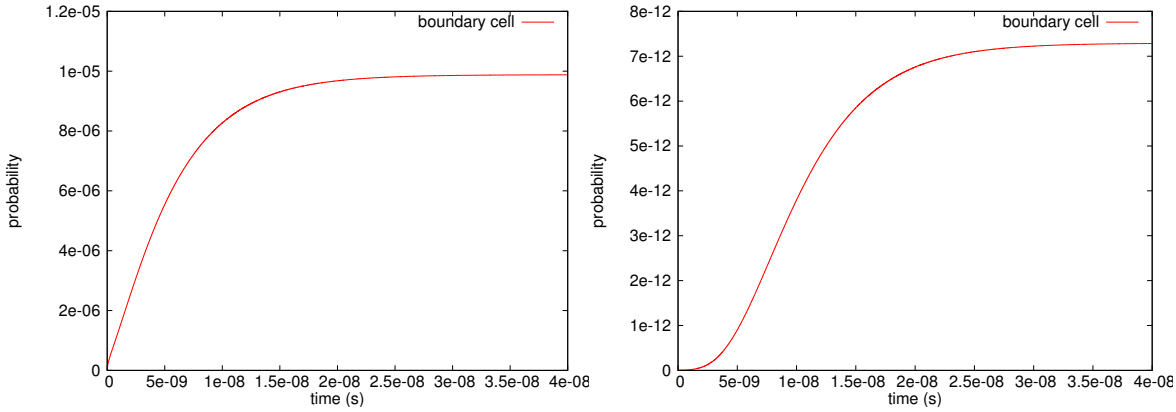
Figure 14: Comparison of source number probabilities for a whole sphere and and outer half spherical shell of a one-dimensional sphere with $k_{eff} = 0.7857$ for θ_2 and θ_{10}.

is higher in the case of the half sphere, this is because we are less likely to detect neutrons in a smaller detection area resulting in this higher extinction probability. Looking at figures 13b, 14a and 14b, similar patterns are shown. It is less likely that neutrons are detected in a smaller detection region and consequently the probabilities in the half sphere are smaller than in the whole sphere. It can be noted that the difference in probabilities increases for increasing n, this is due to the fact it is more difficult to build up large quantities of neutrons in the outer region of the sphere because of leakage across the spheres surface.
Moving on to figures 15a, 15b, 16a and 16b, similar patterns can be seen for the distributions in the boundary cell, however the probability of extinction is much higher and the non-zero number probabilities are much lower - in line with expectation from a much smaller detection region. In all the figures, as time increases the population



(a) θ_0 (b) θ_1

Figure 15: Source number probabilities in a boundary cell of a one-dimensional sphere with $k_{eff} = 0.7857$ for θ_0 and θ_1.



(a) θ_2 (b) θ_{10}

Figure 16: Source number probabilities in a boundary cell of a one-dimensional sphere with $k_{eff} = 0.7857$ for θ_2 and θ_{10}.

becomes such that the spontaneous and induced fission neutrons balance those being removed from the system by leakage and absorption, resulting in the steady state. Note also that this occurs later in time for the larger neutron number, the smaller the detector region, due to the fact that neutrons produced in the interior have to diffuse to this outer region.

Similarly, for $\theta_{10}(s)$ we see that initially the gradient is shallow. This is because the maximum spontaneous fission multiplicity is six, meaning a few time steps are required for the population to feasibly build up to this level, even within the detector cell. The gradient then increases as neutrons from subsequent source emissions and induced fission neutrons diffuse over to the boundary where they start to leak form the system. The probabilities reach a plateau where neutrons produced in spontaneous and induced

fission balance the neutrons removed from the system by leakage and absorption.

As the distributions are uniform in space it is additionally interesting to compare the steady state solutions in the one dimensional spherical model created to its point model counterpart. Table 8 shows the extinction probabilities and figure 17 shows the comparison of the steady state solutions for the individual number probabilities in four different regions for a 3.7938 cm radius sphere of multiplying material with $k_{eff} = 0.7857$, to a point model.

region	point model	entire sphere	outer half	inner half	boundary shell
extinction	0.996484	0.999120	0.999184	0.999682	0.999890

Table 8: Extinction probabilities for different counting regions and the point model.

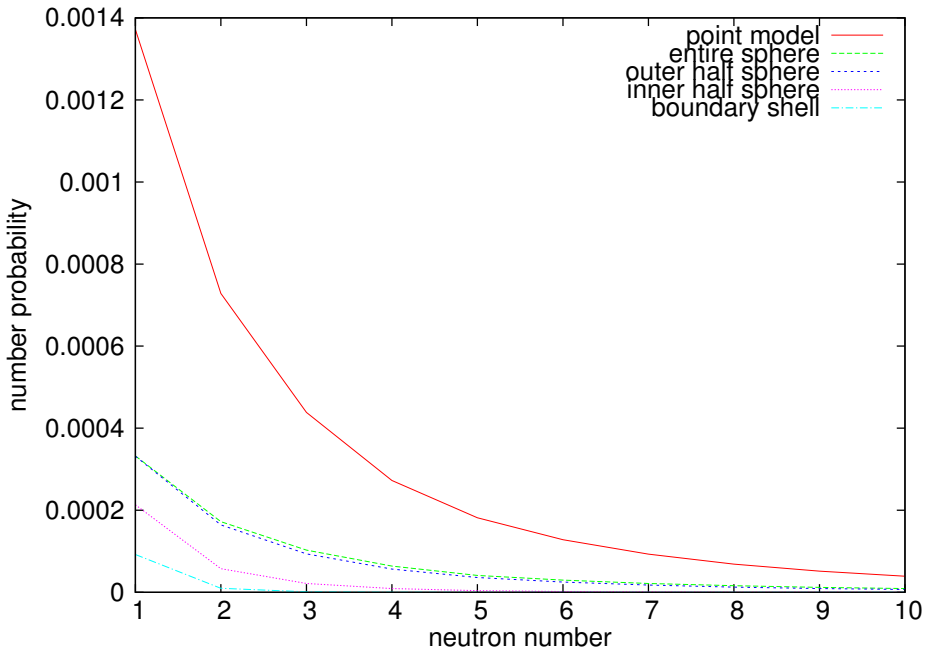


Figure 17: Comparison between the steady state number probabilities of a 3.7938 cm radius sphere of multiplying material in different regions with $k_{eff} = 0.7857$ and the point model with $k_\infty = 0.7857$.

As before, we see the relative sizes of the non-zero probabilities are connected to the volume of each of the detector regions. To highlight this, the outer half spherical shell has 7/8 of the volume of the entire sphere, compared to the inner half sphere which has only 1/8 of the total volume. Consequently, the outer half has very similar non zero probabilities to the entire sphere, whereas those of the inner half are much smaller. As can be seen from figure 17, the point model has higher non-zero number probabilities than the spherical models - this is likely due to the fact that although k_∞ has been adjusted to k_{eff} to incorporate leakage, no adjustment has been made to account for the geometry of the sphere considered in the one dimensional cases.

6.3. Multi-Region Sphere: Single Initiating Neutron

We now extend the bare sphere considered previously to a multi-region model. We begin by considering the distributions for a single initiating neutron; the calculation of which proceeds in exactly the same manner as detailed in the single region model except in that allowance is now made for the cross sections to vary in the different spatial regions.

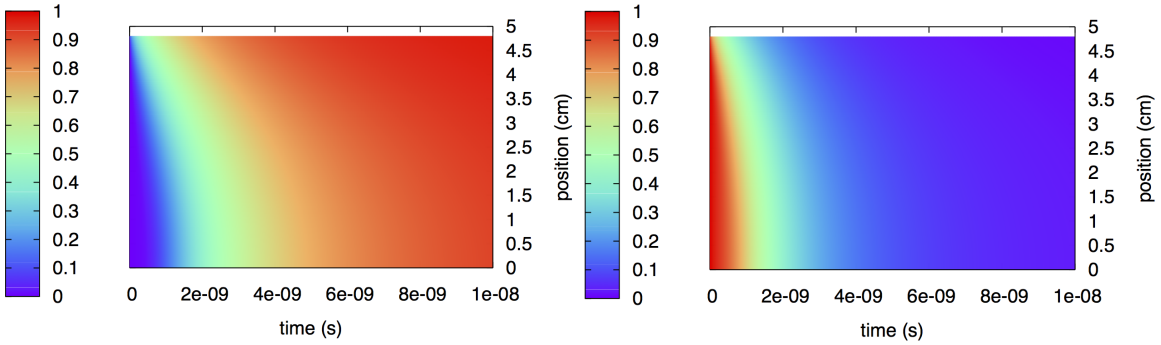
The multi region sphere investigated is similar to that described by Miller et al. (2014), consisting of a 3.7938cm radius source of plutonium, made up of 5.91% Pu^{240} and 93.27% Pu^{239} with the additional mass made up of other isotopes of Pu, surrounded by a 1cm reflector of high density polyethylene with a diffusion length L= 119.81cm, giving an assembly with a k_{eff} of 0.8061. The cross sections in the sphere are as given in table (3) and for the reflector are as shown in table (9). Once again, we note the calculation of ten probabilities accounts for more than 99% of the neutrons within the system.

cross section	Σ_t	Σ_a	Σ_f
	3.8374×10^{-1}	6.0512×10^{-5}	0.0

Table 9: WIMS (2014) generated cross section data for fast neutrons in a diffusion model with isotropic scattering for the reflector considered in this section.

As before, results are shown for three different regions for a 1cm thick reflector: the whole sphere and reflector, the outer boundary of the sphere and the outer boundary of the reflector. The results seen in this section show interesting behaviour in their own right, but are especially interesting when considered in conjunction with the results in the homogeneous sphere case.

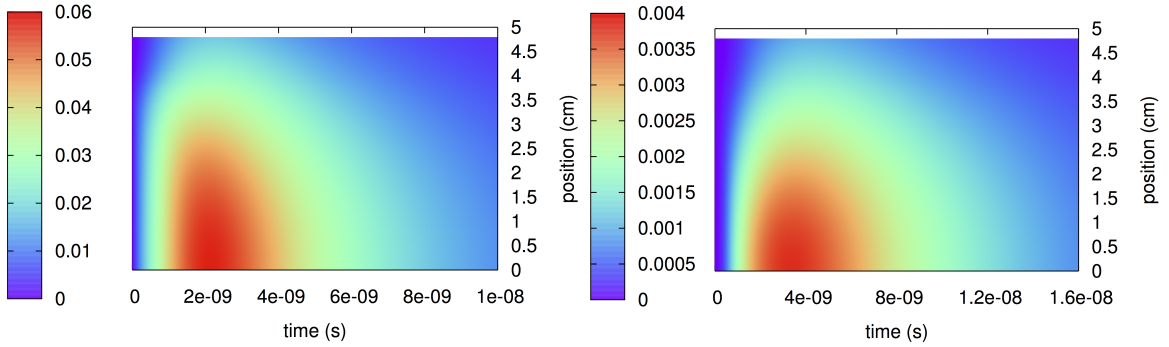
6.3.1. Full Sphere



(a) p_0 (b) p_1

Figure 18: Number probabilities in the whole of a one-dimensional sphere of size 3.7938cm with a 1cm thick reflector for p_0 and p_1.

Firstly consider the extinction probability in the two-region sphere, as given by figure 18a. When compared with its one-region counterpart, the probability is seen



(a) p_2 (b) p_{10}

Figure 19: Number probabilities in the whole of a one-dimensional sphere of size 3.7938cm with a 1cm thick reflector for p_2 and p_{10}.

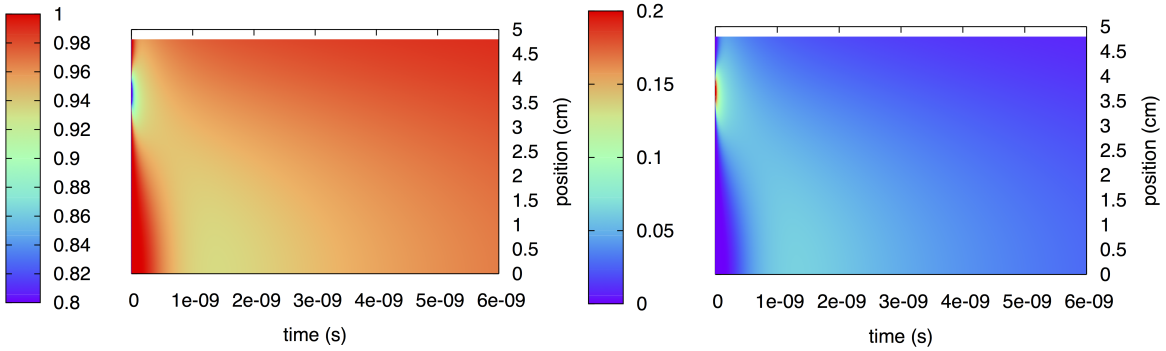
to increase more slowly - this is due to the reflector effectively damping the results. As scattering events are likely to occur in the reflector, the initial neutron - and any produced from subsequent fissions - are likely to remain for longer times, undergoing more events before leaking from the system. Similarly, the distribution in figure 18b shows a slower progression with time when compared to 7b as the reflector causes the neutrons to effectively be more long-lived in the system, through additional scattering events.

Whilst figure 19a shows a slower progression in time than 8a, relatively little difference can be seen in the magnitude of the two graphs. This is especially interesting when looked at in comparison to figures 19b and 8b, where a marked difference is seen. In the case of ten neutrons, the reflector allows for the retention of neutrons in the system - slowing down their path to the sphere's boundary - and also reflects some back into the fissioning medium where before, without the presence of the reflector, they would have leaked from the system. This results in larger probabilities for finding ten neutrons in the system with a reflector than without.

6.3.2. Boundary Cell of Sphere

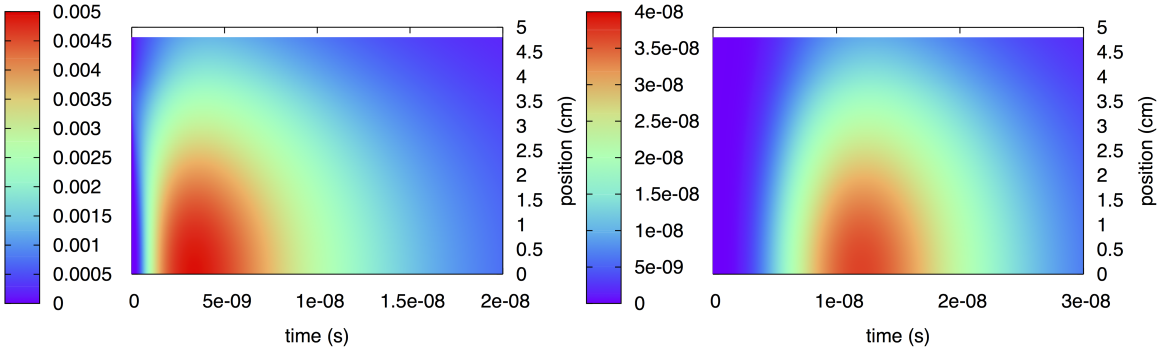
Now consider the single initiating neutron distributions where counting of the neutrons takes place in the outer cell of the multiplying sphere. As given by the initial condition, for figure 20a the probability of finding zero neutrons is one everywhere except when the neutron is injected into the counting region, where it is zero. As expected, the probability increases in the small area around the counting region, with two shadows being present either side. These two shadows relate to where neutrons are injected away from the counting region and then have to diffuse over to this region before being recorded - hence the probability, which is initially one, dropping slightly, before again heading towards one in light of the highly sub-critical system being considered.

A similar pattern is seen in the case of figure 20b to that of the previously shown figures, this is approximately the opposite of the distribution to $p_0(r, s)$, but fits within this distribution allowing for the presence of higher number probabilities.



(a) p_0 (b) p_1

Figure 20: Number probabilities in the boundary cell of a one-dimensional sphere of size 3.7938cm with a 1cm thick reflector for p_0 and p_1.



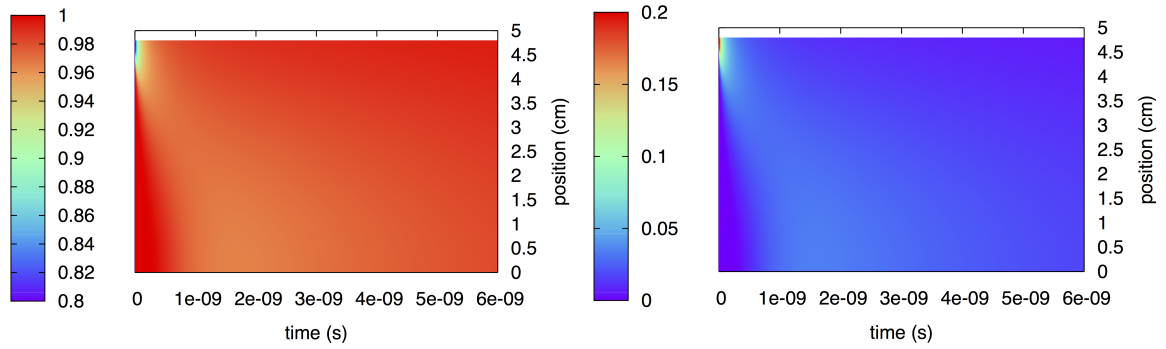
(a) p_2 (b) p_{10}

Figure 21: Number probabilities in the boundary cell of a one-dimensional sphere of size 3.7938cm with a 1cm thick reflector for p_2 and p_{10}.

It is especially interesting to look at the distributions for $p_2(r, s)$ and $p_{10}(r, s)$ in comparison to their counterparts to the boundary cell case in the homogenous sphere. When compared to figures 12a and 12b figures 21a and 21b are much higher in magnitude. This shows that the presence of the reflector has a large effect on the distributions, allowing neutrons to enter the reflecting region, scatter around and then re-renter the counting region. For this reason it can be seen that the distributions are not only greater in magnitude, but also show a slower time progression.

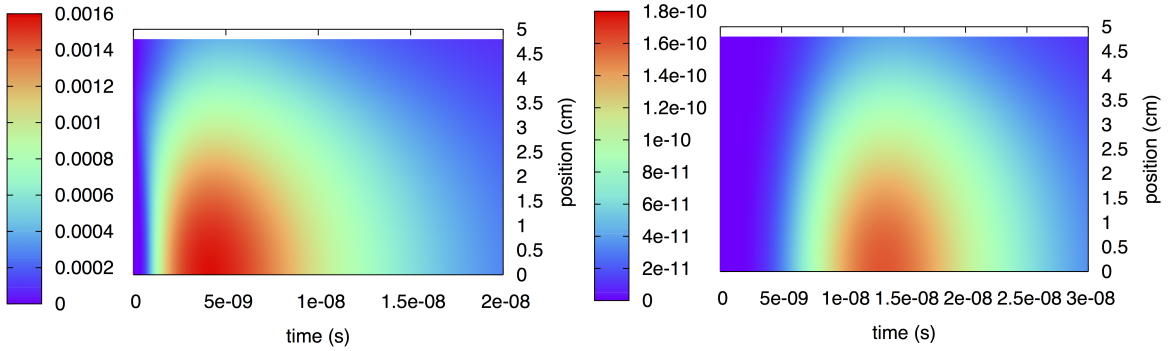
6.3.3. Boundary Cell of Reflector

The boundary cell of the reflector follows a very similar pattern to that of the boundary cell of the sphere in the homogenous case. In this manner, figures 22a, 22b, 23a and 23b replicate the patterns seen in figures 11a, 11b, 12a and 12b. However, these again show a slower time progression due to the reflector causing the neutrons to undergo scattering events before reaching the counting region. It is also important to note that these distributions are slightly higher in magnitude than their homogenous



(a) p_0 (b) p_1

Figure 22: Number probabilities in the outer boundary cell of the reflector for a one-dimensional sphere of size 3.7938cm with a 1cm thick reflector for p_0 and p_1.



(a) p_2 (b) p_{10}

Figure 23: Number probabilities in the outer boundary cell of the reflector for a one-dimensional sphere of size 3.7938cm with a 1cm thick reflector for p_2 and p_{10}.

sphere counterparts - due to the reflector allowing neutrons to leave the sphere and then scatter back into the multiplying region producing more neutrons, although a fairly small effect of this is seen.

6.4. Multi-Region Sphere: Random Intrinsic Source

We now extend the intrinsic source case to a multi-region sphere. In a one-dimensional, multi-region model evaluating Eq.(14a) at $z = 0$, gives

$$\frac{\partial \theta_0(r,s)}{\partial s} = \left[\sum_{k=1}^{K_Q} \frac{(-1)^k}{k!} \chi_k^{(Q)}(r) \int_{r=0}^{r_B} Q(r) 4\pi r^2 dr \frac{3}{4\pi r_B^3} p_s^k(r,s) \right] \theta_0(r,s) \tag{78}$$

with initial condition

$$\theta_0(r,0) = 1 \tag{79}$$

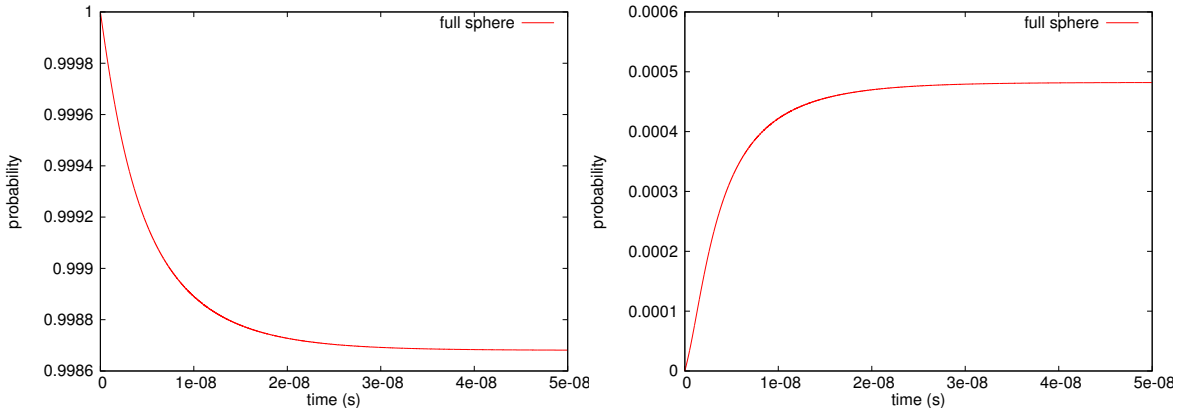
and where r_B is now the radius of the sphere containing the source.

Again, the higher order probabilities can again be extracted via the evaluation of derivatives of $G^{(Q)}$ at $z = 0$ to give the $\theta_n(r, s)$ which are subject to the initial condition

$$\theta_n(r, 0) = 0 \tag{80}$$

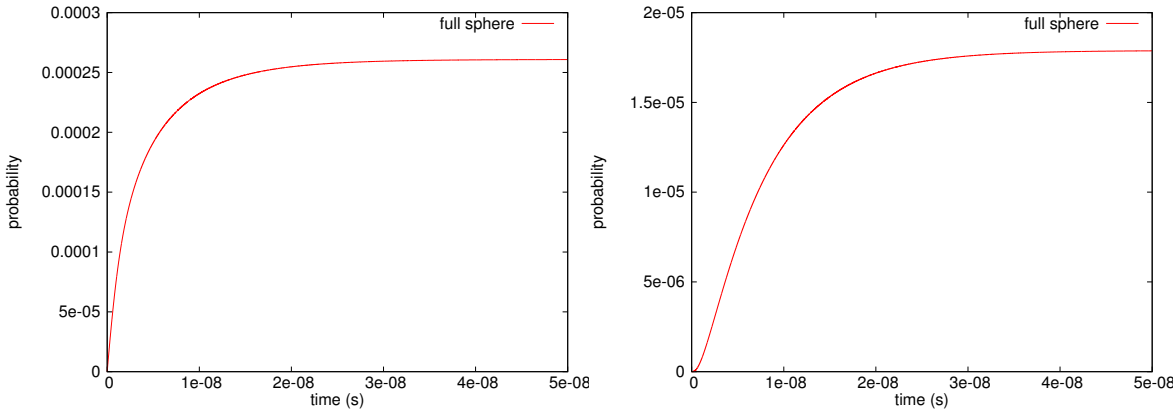
Using the single initiating neutron distributions as an input, Eq.(78) was simply solved using a Crank-Nicholson scheme in time. As the results for the random intrinsic source give a uniform distribution in space within the counting region, the distributions can be plotted in only a time dependent scenario for the three different counting regions considered.

6.4.1. Full Sphere



(a) θ_0 (b) θ_1

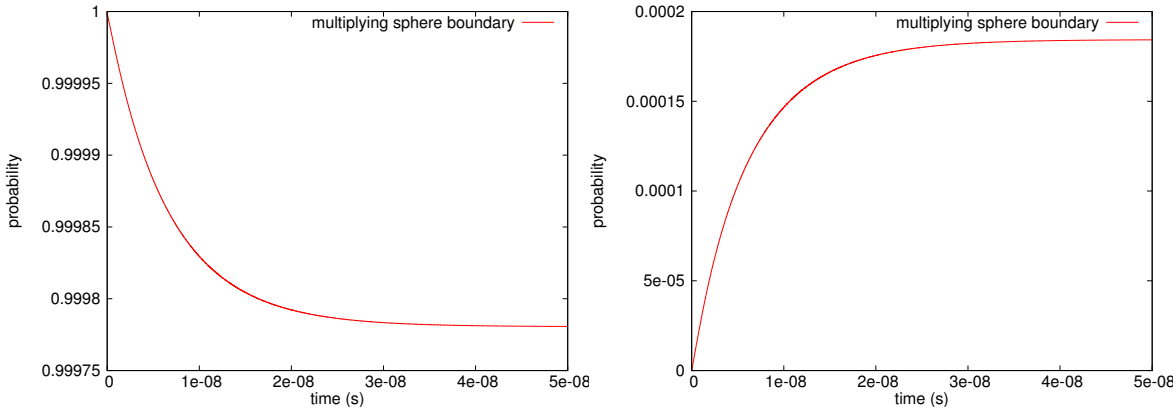
Figure 24: Source number probabilities for whole sphere of a one-dimensional sphere with a 1cm thick reflector for θ_0 and θ_1.



(a) θ_2 (b) θ_{10}

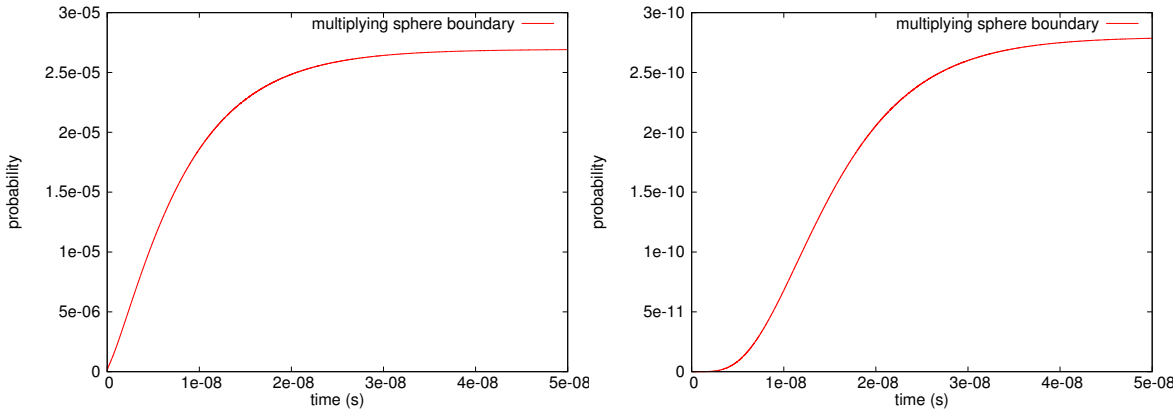
Figure 25: Source number probabilities for whole sphere of a one-dimensional sphere with a 1cm thick reflector for θ_2 and θ_{10}.

6.4.2. Boundary of Multiplying Sphere



(a) θ_0 (b) θ_1

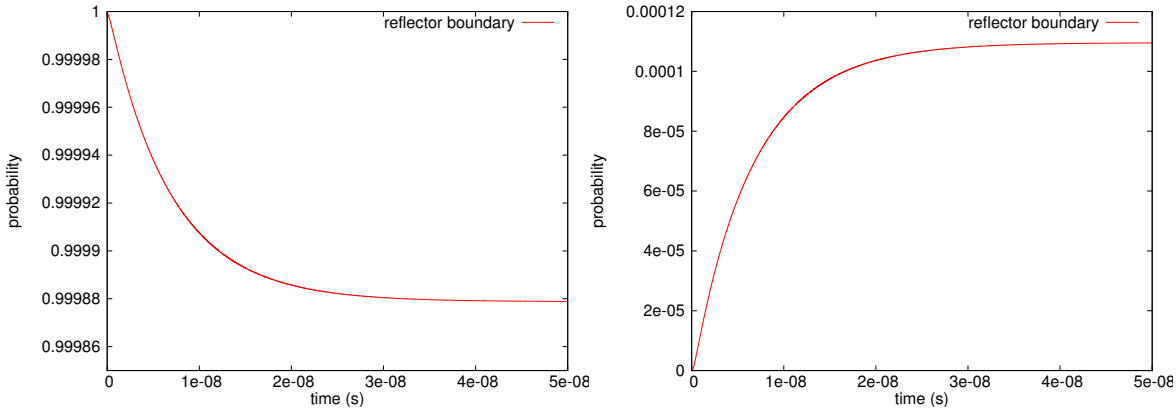
Figure 26: Source number probabilities for the boundary cell of the 3.7938 cm multiplying sphere surrounded by 1 cm reflector for θ_0 and θ_1.



(a) θ_2 (b) θ_{10}

Figure 27: Source number probabilities for the boundary cell of the 3.7938 cm multiplying sphere surrounded by 1 cm reflector for θ_2 and θ_{10}.

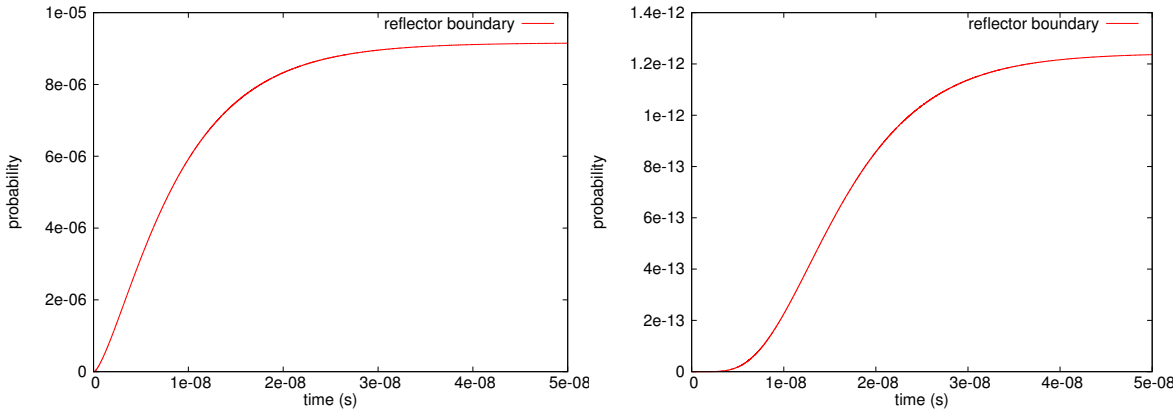
6.4.3. Outer Boundary of Reflector



(a) θ_0 (b) θ_1

Figure 28: Source number probabilities for outer the boundary cell of a 1cm reflector surrounding a 3.7938 cm multiplying sphere for θ_0 and θ_1.

As can be seen from the graphs in figures 24a to 29b, the time evolution of the neutron number probabilities in the presence of a source are very similar, independent of the counting region considered. The differences between the three regions are encapsulated in how rapidly this time evolution takes place and the magnitude of the steady state reached. As would be expected, the largest counting region results in the largest magnitude of non-zero number probabilities, as it will contain the most neutrons. Note also that the magnitude of the source number probabilities in the whole sphere in the case of the reflector is larger than that without - in line with physical intuition. This is additionally seen in the case of the boundary cell, where a marked increase is seen in the boundary cell of the sphere due to the presence of a reflector. In all cases, in



(a) θ_2 (b) θ_{10}

Figure 29: Source number probabilities for outer the boundary cell of a 1cm reflector surrounding a 3.7938 cm multiplying sphere for θ_2 and θ_{10}.

the presence of a reflector, a longer period of time is required to reach a steady state due, again, to the scattering in the reflector delaying and reducing leakage and hence delaying the point at which a balance can be reached between neutrons leaving the system and those produced within the system.

7. Conclusions

In this paper we obtained the solution of the temporally and spatially extensive neutron number probability equations for a randomly emitting source in the diffusion approximation for one dimensional subcritical systems. This has extended previous work which was restricted to a lumped model formulation. Equations for the number probabilities in the single initiating neutron case and for a random intrinsic source were derived and numerically solved in both slab geometry and spherical geometry for neutron number of order up to fifty. A partial benchmark with a semi-analytical solution obtained in slab geometry showed excellent agreement with the model we have created.

This work demonstrates the importance of including spatial dependence in the neutron number probability distributions, showing complex spatial behaviours which cannot be encapsulated in a point model system. This is especially evident in the case of the multi region model where some regions contain a source and others do not. Whilst the results of the calculations performed are interesting and a valuable extension to work already undertaken, we note the limitations of the work completed. Firstly, increasing the accuracy of the calculations performed by refining the spatial mesh and timestep used results in increased computation time. Greater computation efficiency can be achieved by implementing a nonuniform spatial mesh and more advanced discretisation method such as finite elements. Secondly, the equations derived for the number probabilities have very large numbers of terms, making the calculation of the larger probabilities impractical. However, this may be somewhat mitigated by

restricting the length of the fission chains included in the source term calculation and is currently being investigated. Finally the diffusion approximation was employed to simplify the numerical solution of the equations. Whilst this was not an unreasonable approximation to make, a more accurate mathematical model is warranted for the small subcritical systems of interest. We hope in a future communication to present results for the number distribution based on numerical solution of the energy dependent coupled system of transport equations obtained from the generating function equation without approximation.

Acknowledgements

Joanna Saxby would like to acknowledge the support of EPSRC under their industrial doctorate programme (EPSRC grant number: EP/G037426/1) as well as industrial support from the Atomic Weapons Establishment (AWE), Aldermaston, United Kingdom.

Anil K. Prinja would like to acknowledge the financial and logistical support of the Nuclear Engineering Group at Imperial College, London.

M.D. Eaton would like to would like to thank EPSRC for their support through the following grants: "Adaptive Hierarchical Radiation Transport Methods to Meet Future Challenges in Reactor Physics (EPSRC grant number: EP/J002011/1) and "RADIANT: A Parallel, Scalable, High Performance Radiation Transport Modelling and Simulation Framework for Reactor Physics, Nuclear Criticality Safety Assessment and Radiation Shielding Analyses (EPSRC grant number: EP/K503733/1).

The authors are grateful to Emeritus Professor M. M. R. Williams for his helpful comments on this work.

Data Statement

In accordance with EPSRC funding requirements, the data used to generate the figures in this paper can be found at http://doi.org/10.5281/zenodo.437102

References

Abate, J. and Whitt, W. (1992). Numerical inversion of probability generating functions. *Operational Research Letters*, 12:245–251.

Bell, G. I. (1963). Probability distribution of neutrons and precursors in a multiplying assembly. *Annals of Physics*, 21:243 – 283.

Bell, G. I. (1965). On the stochastic theory of neutron transport. *Nuclear Science and Engineering*, 21:390 – 401.

Böhnel, K. (1985). The effect of multiplication on the quantitative determination of spontaneously fissioning isotopes by neutron correlation analysis. *Nuclear Science and Engineering*, 90:75.

Chambers, D. H., Chandrasekaran, H., and Walston, S. E. (2016). Fourier method for calculating fission chain neutron multiplicity distributions. *Nuclear Science and Engineering*, 184:244–253.

Enqvist, A., Pázsit, I., and Pozzi, S. (2006). The number distribution of neutrons and gamma photon generated in a multiplying sample. *Nuclear Instruments & Methods in Physics Research, Section A: Accelerators, Spectrometers, Detectors, and Associated Equipment*, 566:598–608.

Gillespie, D. T. (1992). *Markov Processes: An Introduction for Physical Scientists*. Academic Press.

Hansen, G. E. and Roach, W. H. (1961). Six and sixteen group cross sections for fast and intermediate critical assemblies. Technical report, Los Alamos National Laboratory.

Lewis, E. E. and Miller, W. F. (1993). *Computational Methods of Neutron Transport*. American Nuclear Society.

MATLAB (2012). *MATLAB Version 7.14.0.739 (R2012a)*. Massachusetts: The MathWorks Inc.

Mattingly, J. (2012). Computation of neutron multiplicity statistics using deterministic transport. *IEEE Transactions on Nuclear Science*, 59:314–322.

Miller, E. C., Mattingly, J. K., Clarke, S. D., Solomon, C. J., Dennis, B., Meldrum, A., and Pozzi, S. A. (2014). Computational evaluation of neutron multiplicity measurements of polyethylene-reflected plutonium metal. *Nuclear Science and Engineering*, 176:167–185.

Pál, L. (1962). Statistical theory of the chain reaction in nuclear Reactors: Parts I, II, III. Technical report, Atomic Energy Authority.

Pázsit, I. and Pál, L. (2008). *Neutron Fluctuations: A Treatise on the Physics of Branching Processes*. Elsevier.

Pozzi, S. A., Padovani, E., and Marseguerra, M. (2003). MCNP-PoliMi: a Monte-Carlo code for correlation measurements. *Nuclear Instruments & Methods*, 513:550–558.

Prasad, M. K. and Snyderman, N. J. (2012). Statistical theory of fission chains and generalized poisson neutron counting distributions. *Nuclear Science and Engineering*, 172:300–326.

Prinja, A. K. (2012). Notes on the lumped backward master equation for the neutron extinction/survival probability. Technical report, Los Alamos National Laboratory.

Van Kampen, N. G. (1981). *Stochastic processes in physics and chemistry*. North Holland.

Williams, M. M. R. (2016). Burst wait-times in the caliban reactor using the gamma probability distribution function. *Nuclear Science and Engineering*, 183:116–125.

WIMS (2014). *WIMS: A Modular Scheme for Neutronics Calculations*. AMEC FOSTER WHEELER. User Guide for Version 10 Issue 1.

Appendix A. An Algorithm to Generate the Neutron Number Probability Equations

Having looked at the individual equations for the number probabilities, both in the case of a single initiating neutron and an intrinsic source, it clear that the complexity associated with using the backward approach is encapsulated in the terms produced from the derivatives of the non-linear term in Eq. (21). As a result, in this appendix, we give details of the algorithm developed in order to produce the equations for solution when considering the neutron number probabilities.

Appendix A.1. Single Initiating Nutron

Consider Eqs. (27) (28) and (29). On the whole, these equations have very similar terms: we have an adjoint diffusion equation in $p_1(\vec{r},s)$, $p_2(\vec{r},s)$ or $p_3(\vec{r},s)$ with additional terms created from the differentiation of the non-linear term in Eq. (21). It is these additional terms, which effectively act as a source within the general transport equation, which need to be modelled by the algorithm created.

Consider, now, the differentiation of the non-linear term in Eq. (21) as given by

$$\frac{\partial}{\partial z}\left[\Sigma_f(\vec{r})\sum_{k=2}^{K}\frac{(-1)^k}{k!}\chi_k\tilde{G}^k(z;\vec{r},s)\right]=\frac{\partial}{\partial z}K\big(\tilde{G}(z)\big) \tag{A.1}$$

To differentiate Eq. (A.1), requires the use of a chain rule, via

$$\begin{aligned}\frac{\partial}{\partial z}\Big[K\big(\tilde{G}(z)\big)\Big] &= \frac{\partial K}{\partial\tilde{G}}\frac{\partial\tilde{G}}{\partial z}\\ &= \left[\Sigma_f(\vec{r})\sum_{k=2}^{K}\frac{(-1)^k}{(k-1)!}\chi_k\tilde{G}(z;\vec{r},s)^{k-1}\right]\times\frac{\partial\tilde{G}(z;\vec{r},s)}{\partial z}\end{aligned} \tag{A.2}$$

Where we note that the bracketed quantity strongly resembles the original function, $K(\tilde{G})$ whilst the other constituent is simply the differentiation of $\tilde{G}$ with respect to z. We now re-write the terms as

$$\begin{aligned}K((\tilde{G})=\mathcal{K}(0)&=\left[\Sigma_f(\vec{r})\sum_{k=2}^{K}\frac{(-1)^k}{k!}\chi_k\tilde{G}^k(z;\vec{r},s)\right]\\ \mathcal{P}(0)&=\tilde{G}(z;\vec{r},s)\end{aligned} \tag{A.3}$$

noting the resemblance to the original functions, we then write the derivative terms as

$$\begin{aligned}\mathcal{K}(1)&=\Sigma_f(\vec{r})\sum_{k=2}^{K}\frac{(-1)^k}{(k-1)!}\chi_k\tilde{G}(z;\vec{r},s)^{k-1}\\ \mathcal{P}(1)&=\frac{\partial\tilde{G}(z;\vec{r},s)}{\partial z}\end{aligned} \tag{A.4}$$

and so on, such that generally

$$\begin{aligned}\mathcal{K}(j) &= \sum_{k=2}^{K} \frac{(-1)^k}{(k-j)!} \chi_k \tilde{G}(z;\vec{r},s)^{k-j} \\ \mathcal{P}(j) &= \frac{\partial^j \tilde{G}(z;\vec{r},s)}{\partial z^j}\end{aligned} \tag{A.5}$$

so that Eq. (A.2) can be compactly re-written as

$$\frac{\partial}{\partial z}\mathcal{K}(0) = \mathcal{K}(1)\mathcal{P}(1) \tag{A.6}$$

In this way, when differentiated with respect to z, these two types of terms have the following relationships, for $\mathcal{K}(j)$

$$\begin{aligned}\frac{\partial}{\partial z}\mathcal{K}(1) &= \mathcal{K}(2)\mathcal{P}(1) \\ \frac{\partial}{\partial z}\mathcal{K}(2) &= \mathcal{K}(3)\mathcal{P}(1) \\ &\cdots \\ \frac{\partial}{\partial z}\mathcal{K}(j) &= \mathcal{K}(j+1)\mathcal{P}(1)\end{aligned} \tag{A.7}$$

and for $\mathcal{P}(j)$

$$\begin{aligned}\frac{\partial}{\partial z}\mathcal{P}(1) &= \mathcal{P}(2) \\ \frac{\partial}{\partial z}\mathcal{P}(2) &= \mathcal{P}(3) \\ &\cdots \\ \frac{\partial}{\partial z}\mathcal{P}(j) &= \mathcal{P}(j+1)\end{aligned} \tag{A.8}$$

If products of these two types of term are being differentiated, the product rule can be trivially applied as is the case when considering the n^{th} derivatives of the function $\mathcal{K}(0)$.

The first part of the algorithm performs exactly this for the $(n+1)^{th}$ derivative by "reading" a term from the n^{th} derivative and then systematically working through each constituent of the product and applying the rules detailed in Eqs. (A.7) and (A.8) whilst keeping the other constituents of the product the same. Performing this, the first step of the algorithm generates

$$
\begin{aligned}
\frac{\partial}{\partial z}\mathcal{K}(0) &= \mathcal{K}(1)\mathcal{P}(1) \\
\frac{\partial^2}{\partial z^2}\mathcal{K}(0) &= \mathcal{K}(2)\mathcal{P}(1)\mathcal{P}(1) + \mathcal{K}(1)\mathcal{P}(2) \\
\frac{\partial^3}{\partial z^3}\mathcal{K}(0) &= \mathcal{K}(3)\mathcal{P}(1)\mathcal{P}(1)\mathcal{P}(1) + \mathcal{K}(2)\mathcal{P}(2)\mathcal{P}(1) + \mathcal{K}(2)\mathcal{P}(1)\mathcal{P}(2) \\
&\quad + \mathcal{K}(2)\mathcal{P}(1)\mathcal{P}(2) + \mathcal{K}(1)\mathcal{P}(3)
\end{aligned}
\tag{A.9}
$$

where the scale of escalation of the number of terms, becomes clear for each successive differentiation. In light of this, it is obvious that like terms should be collected, thus the next step of the algorithm orders the terms as

$$
\begin{aligned}
\frac{\partial}{\partial z}\mathcal{K}(0) &= \mathcal{K}(1)\mathcal{P}(1) \\
\frac{\partial^2}{\partial z^2}\mathcal{K}(0) &= \mathcal{K}(2)\mathcal{P}(1)\mathcal{P}(1) + \mathcal{K}(1)\mathcal{P}(2) \\
\frac{\partial^3}{\partial z^3}\mathcal{K}(0) &= \mathcal{K}(3)\mathcal{P}(1)\mathcal{P}(1)\mathcal{P}(1) + \mathcal{K}(2)\mathcal{P}(2)\mathcal{P}(1) + \mathcal{K}(2)\mathcal{P}(2)\mathcal{P}(1) \\
&\quad + \mathcal{K}(2)\mathcal{P}(2)\mathcal{P}(1) + \mathcal{K}(1)\mathcal{P}(3)
\end{aligned}
\tag{A.10}
$$

so that the third step of the algorithm can collect like terms as

$$
\begin{aligned}
\frac{\partial}{\partial z}\mathcal{K}(0) &= \mathcal{K}(1)\mathcal{P}(1) \\
\frac{\partial^2}{\partial z^2}\mathcal{K}(0) &= \mathcal{K}(2)\mathcal{P}(1)\mathcal{P}(1) + \mathcal{K}(1)\mathcal{P}(2) \\
\frac{\partial^3}{\partial z^3}\mathcal{K}(0) &= \mathcal{K}(3)\mathcal{P}(1)\mathcal{P}(1)\mathcal{P}(1) + 3\mathcal{K}(2)\mathcal{P}(2)\mathcal{P}(1) + \mathcal{K}(1)\mathcal{P}(3)
\end{aligned}
\tag{A.11}
$$

The $\mathcal{K}$, $\mathcal{P}$ and coefficient terms are then stored in three two-dimensional matrices such that the n^{th} row represents the terms of the n^{th} derivative with new terms in the summation being indicated by the presence of a 0.

As such, if we were to re-write the terms in Eq. (A.11) in these three matrices $\mathbb{K}$, $\mathbb{P}$ and $\mathbb{C}$ they would take the following form

$$
\mathbb{P} = \begin{pmatrix} 1 & 0 & 0 & 0 & 0 & 0 & 0 & 0 \\ 1 & 1 & 0 & 2 & 0 & 0 & 0 & 0 \\ 1 & 1 & 1 & 0 & 2 & 1 & 0 & 3 \end{pmatrix} \qquad \mathbb{K} = \begin{pmatrix} 1 & 0 & 0 & 0 & 0 & 0 & 0 & 0 \\ 2 & 0 & 0 & 1 & 0 & 0 & 0 & 0 \\ 3 & 0 & 0 & 0 & 2 & 0 & 0 & 1 \end{pmatrix} \tag{A.12}
$$

$$
\mathbb{C} = \begin{pmatrix} 1 & 0 & 0 & 0 & 0 & 0 & 0 & 0 \\ 1 & 0 & 0 & 1 & 0 & 0 & 0 & 0 \\ 1 & 0 & 0 & 0 & 3 & 0 & 0 & 1 \end{pmatrix}
$$

As a verification of the validity of the algorithm constructed, the first eight equations were compared to those in table A.I of Böhnel (1985) and were in agreement.

Note that in order to transform these equations for the differentials of the generating function into equations for the neutron number probabilities, these expressions need to be evaluated at $z = 0$ which has the result of changing the signs of the terms in the summation, dependent on the $\mathcal{K}$ term: odd numbers here equate to a minus and even numbers to a plus.

In the case of the intrinsic source, a similar process was undertaken. Consider now Eq. (16a). Similarly to the single initiating neutron case, this has a nested part - with the same structure as $\mathcal{K}$ which will create new $\mathcal{K}$ terms - which we will denote $\mathcal{K}^{(Q)}$ as they are *not* identical to the $\mathcal{K}$ terms in the single initiating neutron case - and an additional $\mathcal{P}$ term, but this time it is multiplied by a Θ term. The form of the equation to be differentiated is therefore

$$\frac{\partial}{\partial z}\mathcal{K}^{(Q)}(0)\Theta(0) = \frac{\partial \mathcal{K}^{(Q)}(0)}{\partial z}\Theta(0) + \mathcal{K}^{(Q)}(0)\frac{\partial \Theta(0)}{\partial z} \tag{A.13}$$

where this time the $\mathcal{K}^{(Q)}$ terms are defined as

$$\mathcal{K}^{(Q)}(j) = \sum_{k=1}^{K_Q} \frac{(-1)^k}{(k-j)!}\chi_k^{(Q)} \int w(\vec{r})\tilde{G}(z;\vec{r},s)^{(k-j)} \tag{A.14}$$

and undertake the same pattern in differentiation as in Eq. (A.10), and where we have used a simple product rule. Additionally we note that

$$\begin{aligned}
\frac{\partial}{\partial z}\Theta(0) &= \Theta(1) = \frac{\partial G^{(Q)}}{\partial z} \\
\frac{\partial}{\partial z}\Theta(1) &= \Theta(2) = \frac{\partial^2 G^{(Q)}}{\partial z^2} \\
&\cdots \\
\frac{\partial}{\partial z}\Theta(j) &= \Theta(j+1) = \frac{\partial^{(j+1)} G^{(Q)}}{\partial z^{(j+1)}}
\end{aligned} \tag{A.15}$$

Such that Eq. (A.13) can be written as

$$\frac{\partial}{\partial z}\mathcal{K}(0)\Theta(0) = \mathcal{K}^{(Q)}(1)\mathcal{P}(1)\Theta(0) + \mathcal{K}^{(Q)}(0)\Theta(1) \tag{A.16}$$

similarly the next few derivatives become

$$\begin{aligned}\frac{\partial^2}{\partial z^2}\mathcal{K}^{(Q)}(0)\Theta(0) &= \mathcal{K}^{(Q)}(2)\mathcal{P}(1)\mathcal{P}(1)\Theta(0) + \mathcal{K}^{(Q)}(1)\mathcal{P}(2)\Theta(0) + 2\mathcal{K}^{(Q)}(1)\mathcal{P}(1)\Theta(1) \\ &\quad + \mathcal{K}^{(Q)}(0)\Theta(2) \\ \frac{\partial^3}{\partial z^3}\mathcal{K}^{(Q)}(0)\Theta(0) &= \mathcal{K}^{(Q)}(3)\mathcal{P}(1)\mathcal{P}(1)\mathcal{P}(1)\Theta(0) + 3\mathcal{K}^{(Q)}(2)\mathcal{P}(2)\mathcal{P}(1)\Theta(0) \\ &\quad + 3\mathcal{K}^{(Q)}(2)\mathcal{P}(1)\mathcal{P}(1)\Theta(1) + \mathcal{K}^{(Q)}(1)\mathcal{P}(3)\Theta(0) + 3\mathcal{K}^{(Q)}(1)\mathcal{P}(2)\Theta(1) \\ &\quad + 2\mathcal{K}^{(Q)}(1)\mathcal{P}(1)\Theta(2) + \mathcal{K}^{(Q)}(0)\Theta(3)\end{aligned} \tag{A.17}$$

By the comparison of Eq. (A.16) with (A.11), it is clear that the equations are much more lengthy in the case of the intrinsic source. The algorithm created no longer works through differentiation and collection but is simplified by noting that the terms which contain $\Theta(0)$ are the same as the terms in Eq. (A.11), but with the addition of a $\Theta(0)$ term, and that for the remaining terms, only the $\Theta(j)$ terms from the previous order have to be increased to $\Theta(j+1)$. Consequently the algorithm copies terms from the corresponding order in the single initiating neutron case, adding a $\Theta(0)$ and then copies terms from the previous intrinsic source order, increasing the $\Theta(j)$ by one. This process requires an additional matrix to store the Θ terms and as $\Theta(0)$ terms are now present, new terms are indicated in the intrinsic source by a high number, much greater than the order being calculated. The resultant equations were checked against the first ten hand derived equations and were consistent.